Taylor & Francis
Taylor & Francis Group

International Geology Review

ISSN: (Print) (Online) Journal homepage: https://www.tandfonline.com/loi/tigr20

New U-Pb zircon geochronological data for Takestan magmatic rocks (Western Alborz) and their significance for the interpretation of Paleogene magmatism in Iran

Ali A. Sepahi, Batool Nemati, Abbas Asiabanha, David R. Lentz & Chris R. M. McFarlane

To cite this article: Ali A. Sepahi, Batool Nemati, Abbas Asiabanha, David R. Lentz & Chris R. M. McFarlane (10 Dec 2023): New U-Pb zircon geochronological data for Takestan magmatic rocks (Western Alborz) and their significance for the interpretation of Paleogene magmatism in Iran, International Geology Review, DOI: 10.1080/00206814.2023.2291779

To link to this article: https://doi.org/10.1080/00206814.2023.2291779

INTERNATIONAL GEOLOGY REVIEW
https://doi.org/10.1080/00206814.2023.2291779

New U-Pb zircon geochronological data for Takestan magmatic rocks (Western Alborz) and their significance for the interpretation of Paleogene magmatism in Iran

Ali A. Sepahi[a,b], Batool Nemati[a], Abbas Asiabanha[c], David R. Lentz[d] and Chris R. M. McFarlane[c]

[a]Department of Geology, Bu-Ali Sina University, Hamedan, Iran; [b]Department of Geology, Faculty of Science, Ferdowsi University of Mashhad, Mashhad, Iran; [c]Department of Geology, Imam Khomeini International University, Qazvin, Iran; [d]Department of Earth Sciences, University of New Brunswick, Feredericton, Canada

ABSTRACT

The Takestan area is in the western part of the Alborz magmatic arc. Magmatic rocks of the area consist of plutonic rocks (e.g. granitoids), effusive volcanic, and pyroclastic rocks. Using U-Pb zircon LA ICP-MS dating, we conclude that major parts of Takestan plutonic rocks were emplaced at 41–39 Ma (Late Eocene, Bartonian), but a small part of these rocks have ages of ~37 Ma (Late Eocene, Priabonian). The dacitic rocks have an age of ~39 Ma (Late Eocene, Bartonian) and the rhyolitic rocks are the youngest part of the magmatic rocks of the region with ages of 37–35 Ma (Late Eocene, Priabonian). Old zircons are present in all of granitoid and volcanic samples, except for a dacitic sample. They are interpreted both as earlier components in a long-lived magma chamber and inherited zircons from older continental crust. The age of magmatic rocks in the western part of the Alborz magmatic arc decreases from east to west, but the ages of the majority of them are limited to Palaeogene. The studied rocks like other Palaeogene magmatic rocks of Iran were possibly formed in a subduction related tectonic environment. Indeed, the Palaeogene magmatism of Iran is akin to geodynamic events related to Neotethyan subduction beneath Iranian microcontinent at the southern part of Eurasia.

ARTICLE HISTORY
Received 19 July 2023
Accepted 2 December 2023

KEYWORDS
Alborz magmatic arc; granitoid; Iran; Neotethyan ocean; Palaeogene

Introduction

Numerous magmatic events have affected the Iranian crust through geological history. The most important event is in the Cenozoic, which generated a large volume of pyroclastic, volcanic, and plutonic rocks ranging from mafic to felsic, especially in the Palaeogene. This widespread magmatism in Iran is mainly represented by (1) the Urumieh-Dokhtar magmatic arc (UDMA), extending from NW to SE of Iran, (2) the Alborz magmatic arc (AMA) in the north of Iran from E to W and (3) in the Lut Block in the east of Iran (Figure 1). This magmatic event is attributed to tectonic episodes related to subduction of the Arabian plate under Central Iran (e.g. Berberian *et al*. 1982; Shahabpour 2007; among others), slab break-off (Ghasemi and Talbot 2006), slab rollback (Jahangiri 2007) and post-collisional relaxation mechanism (Aghazadeh *et al*. 2011; Rabiee *et al*. (2022) believe that diachronous collision along the Arabia-Eurasia collision zone can be responsible for Cenozoic magmatism and related metallogeny in Iran. In this paper, our focus is manly on the magmatism in the AMA. The AMA is a linear mountain range formed during the early-middle Oligocene. This mountain range subsequently was deformed during the Miocene when uplift of the Kopeh Dagh Basin produced the Kopeh Dagh Mountains (NE of Iran) and continuous shortening resulted in the northward deflection of the eastern Alborz Mountains (Hollingsworth *et al*. 2010).

The northern sectors of the Arabia-Eurasia collision zone are characterized by a system of strongly curved intracontinental ranges that from west to east include the following mountain ranges: The Talesh (NW of Iran), Alborz, and Kopeh Dagh Mountains (Cifelli *et al*. 2015). The palaeomagnetic studies by Mattei *et al*. (2017) indicate that the Alborz Mountains are a secondary arc that originated as a linear mountain belt in the northern part of Iran. The Alborz-Kopeh Dagh zone in north and northeastern Iran began to bend during the Cenozoic, because of the collision of the Arabian-Eurasian plate (Madanipour *et al*. 2017). The curved geometry of the Alborz Mountains is a result of the interaction with the rigid South Caspian Block during the Arabia-Eurasia continental collision (Berberian and King 1981; Allen *et al*. 2003; Brunet *et al*. 2003; Allen 2010; Madanipour *et al*. 2013).

CONTACT Ali A. Sepahi aasepahi@gmail.com; sepahi@basu.ac.ir Department of Geology, Bu-Ali Sina University, Hamedan, Iran
Supplemental data for this article can be accessed online at https://doi.org/10.1080/00206814.2023.2291779

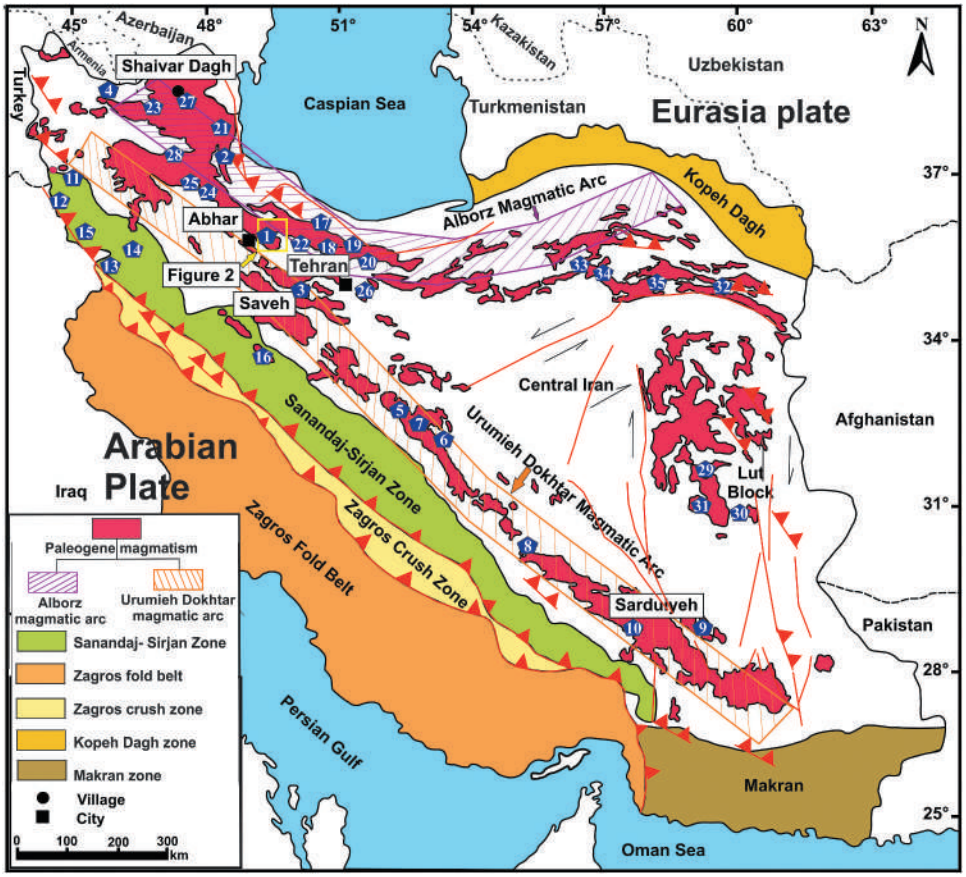

Figure 1. Simplified geological map of Iran displaying major tectono-stratigraphic units of Iran and Paleogene magmatic rocks (modified from Stöcklin 1968; Azizi *et al.* 2018). 1: takestan (the study area); 2: Talesh area; northern part of the UDMA including samples 3 (andesite northwest of Saveh) and 4 (diorite and granodiorite (Shahjahan batholith); southeast UDMA including samples 5 (volcanic samples in Nain), 6 (andesites samples and tuff beside the Batlaqe-Gavkhuni), 7 (andesite in southeast of Nain), 8 (andesitic lava north of the Sirjan), 9 (plutonic and volcanic samples south of Bam) and 10 (Sarduiyeh granitoid); northern part of the Sanandaj–Sirjan zone including samples 11 (Naghadeh granitoid), 12 (intrusive rocks of the Piranshahr), 13 (Marivan granitoid), 14 (Taa–Baysaran of Kamyaran granitoids), 15 (Baneh granites) and 16 (Gosheh–Tavandasht quartz monzodiorite); Alborz magmatic arc including samples 2 (basalts and an andesite from the Talesh), 17 (Akapol quartz monzonite), 18 (andesites of Karaj Formation), 19 (tuff and shale along the Chalus road transect), 20 (Lavasan intrusive body), 21 (basaltic samples in Sabalan–Astara areas), 22 (basaltic andesite from the southwest of Qazvin), 23 (subalkali basalts and andesites from SE Ahar), 24 (Zaker quartz monzonite), 25 (Zanjan quartz monzodiorite), 26 (Ghasrefirozeh granitoid), 27 (granodioritic rocks from Arasbaran) and 28 (Siah-Kamar Mo deposit in Mianeh); Lut block samples including 29 (Koudakan granitoid), 30 (Mahoor granitoid) and 31 (Simorgh granite porphyry dikes); NE of Iran samples including 32 (Aliabad Daman granitoid), 33 (Sabzevar granitoids), 34 (dacitic rocks in Sabzevar) and 35 (Kashmar granitoid).

Paleomagnetic data demonstrate that Alborz range is a secondary arc, and hence, it can be described as an orocline (Mattei *et al.* 2017). Also, these data indicate that this orogen has been primarily formed as a nearly straight E-W oriented range and acquired its present-day curved shape by means of opposite vertical axis rotations from 7.6 Ma (oroclinal bending) (Cifelli *et al.* 2015).

Rabiee *et al.* (2020) proposed that the Cenozoic collisional magmatism and the associated mineralization at the junction of NW-Iran and Caucasus is akin to the activity of a major, lithosphere-scale inherited boundary, transverse to the convergence zone. In such a geodynamic setting, the along-strike segmentation of the lithosphere slab generated asthenospheric melts, their upwelling into the metasomatized supra-subduction mantle wedge and the possible activation of diverse mantle and crustal sources, with consequent mineralization in the region.

The Cenozoic and present-day shortening resulted from the Arabia-Eurasia convergence in Iran is accommodated by mobile belts that surround relatively aseismic crustal blocks (Central Iran, South Caspian, and Lut blocks). These crustal blocks behave as relatively rigid blocks and contributed little to the regional shortening (Mattei *et al.* 2017). In Iran, the tectonic events that accommodate the Cenozoic and present-day shortening include intracontinental mountain building in the Talesh, Zagros, Alborz, and Kopeh Dagh ranges and subduction beneath the central Caspian Sea (Aspheron-Balkhan Sill) and Makran, and also N-S trending right-lateral fault systems in central and eastern Iran (Mattei *et al*. 2017).

According to Barrier *et al*. (2018) the major part of the basin inversion and rock exhumation, recorded along the Caucasus-Talesh-Alborz during the Eocene-Oligocene boundary, is related to the final closure of the Neotethys oceanic way in the Caucasus. This major compressional stage is sign of the transition from back-arc extension to collisional tectonics in the region (Vincent *et al*. 2007; Madanipour *et al*. 2013; Rolland 2017; Van der Boon *et al*. 2018). This latter episode is also referred to the transition from a soft (mostly involving ocean-continent transition margins) to a hard (mature, continent-continent) stage of collision (Ballato *et al*. 2008; Cowgill *et al*. 2016). The shortening and thickening of the Iranian continental crust increased after a so-called "hard collision" at ~20 Ma, which caused a higher rate of deformation, crustal thickening and uplift (Madanipour et al. 2013, 2017), adakitic magmatism and formation of magmatic Cu deposits in south-east UDMA.

Ahmadi *et al*. (2021) has proposed that the collision between the Arabian and central Iran block occurred between middle to upper Eocene and this collision caused crustal thickening in the NW Iran. In addition, Amidi *et al*. (1984) and Dargahi *et al*. (2010) proposed post-collision affinity for some intrusions in the UDMA.

In response to the closure of Neotethys and the continental collision between the Arabian-Eurasian plates, two magmatic arcs were formed: Urumieh-Dokhtar magmatic arc (UDMA) and Alborz magmatic arc (AMA). These magmatic arcs were generated during the subduction of Neotethys oceanic lithosphere to the northeast beneath central Iran block (Omrani *et al*. 2008). Oceanic subduction was accompanied by formation of a cordilleran-type margin along the Sanandaj–Sirjan zone (SSZ) during the Jurassic–Cretaceous (e.g. Berberian and Berberian 1981; Berberian *et al*. 1982; Ghasemi and Talbot 2006; Agard et al. 2006, 2011; Arvin *et al*. 2007; Omrani et al. 2008, 2013), and by the polyphase Cretaceous opening of various back-arc oceanic basins in the overriding plate (i.e. the Sabzevar, Nain-Baft, Sistan Oceans; Arvin and Robinson 1994; McCall 1997; Stampfli and Borel 2002; Bagheri and Stampfli 2008; Shafaii Moghadam et al. 2009, 2013; Rossetti *et al*. 2010; Saccani *et al*. 2010; Nasrabady *et al*. 2011; Omrani *et al*. 2013). But Shafaii Moghadam *et al*. (2023), believe that the magmatism in Alborz-Azerbaijan in the northwest and Torud-Sabzevar in the northeast (parts of the UDMA) are related to the back-arc (or rear-arc) magmatic activity and lie ~ 100 to 600 km behind the volcanic front. According to some other researchers (Sengör *et al*. 1988; McCall 1997; Bagheri and Stampfli 2008; Rossetti *et al*. 2010) the Sabzevar structural zone consists of an orogenic suture zone formed at the expenses of a Cretaceous oceanic domain (the Sabzevar Ocean) and created in the back-arc domain of the Neotethyan subduction.

Northward subduction of Neotethyan oceanic lithosphere was accompanied by strong extension on the upper plate during Late Cretaceous and Palaeogene. This extension stopped when the collision between the Arabian-Eurasia Plates occurred at the beginning of the Neogene (~25 Ma) (Sepidbar *et al*. 2019). However, according to Polliand *et al*. (2005) and Khademi *et al*. (2019), dextral strike-slip fault systems produced the local extensional basin or transtensional zones simultaneous with the collision, enabling magma ascent to the higher levels of the crust.

The Takestan region is in the western part of the AMA and includes various granitoids, volcanic rocks, and pyroclastic units (Figure 2). Except to some preliminary studies, such as 1: 250,000 Qazvin-Rasht geological map (Annells *et al*. 1975) and 1: 100,000 Takestan geological map (Alai Mahabadi and Fanoudi 1992), and limited studies by (Foudazi *et al*. 2015) on the plutonic rocks, a comprehensive geological study and dating of these rocks have not been done previously. Therefore, in this study, we tried to gather U-Pb age data and reveal the geochronological relationship between volcanic and plutonic rocks in this area. Then, we compared our obtained ages with previous data from other similar contemporaneous localities of Iran, which reported Palaeogene magmatism. Our results indicate more evidence for the occurrence of widespread Palaeogene magmatic events in Iran. Furthermore, these results could be used for geodynamic interpretations of Iran during the Palaeogene period.

Geological setting

The Iranian plateau constitutes a main part of Alpine-Himalayan orogenic belt (Berberian and King 1981; Stampfli and Borel 2002; Agard *et al*. 2011 (Figure 1)). The geological history of Iran preserves evidence of the opening and closure of Paleotethys and Neotethys oceans. The opening of the Neotethys in Permo-Triassic has led to the closure of the Paleotethys, the closure of the Paleotethys in the Triassic to the north was accompanied by the movement of the Iranian subcontinent and its joining to the Eurasian plate (Berberian and Berberian 1981; Berberian *et al*. 1982). The final stage of the closure of Neotethys and the collision between the Arabian plate and the Central Iran block occurred during the Neogene (Berberian and Berberian 1981;

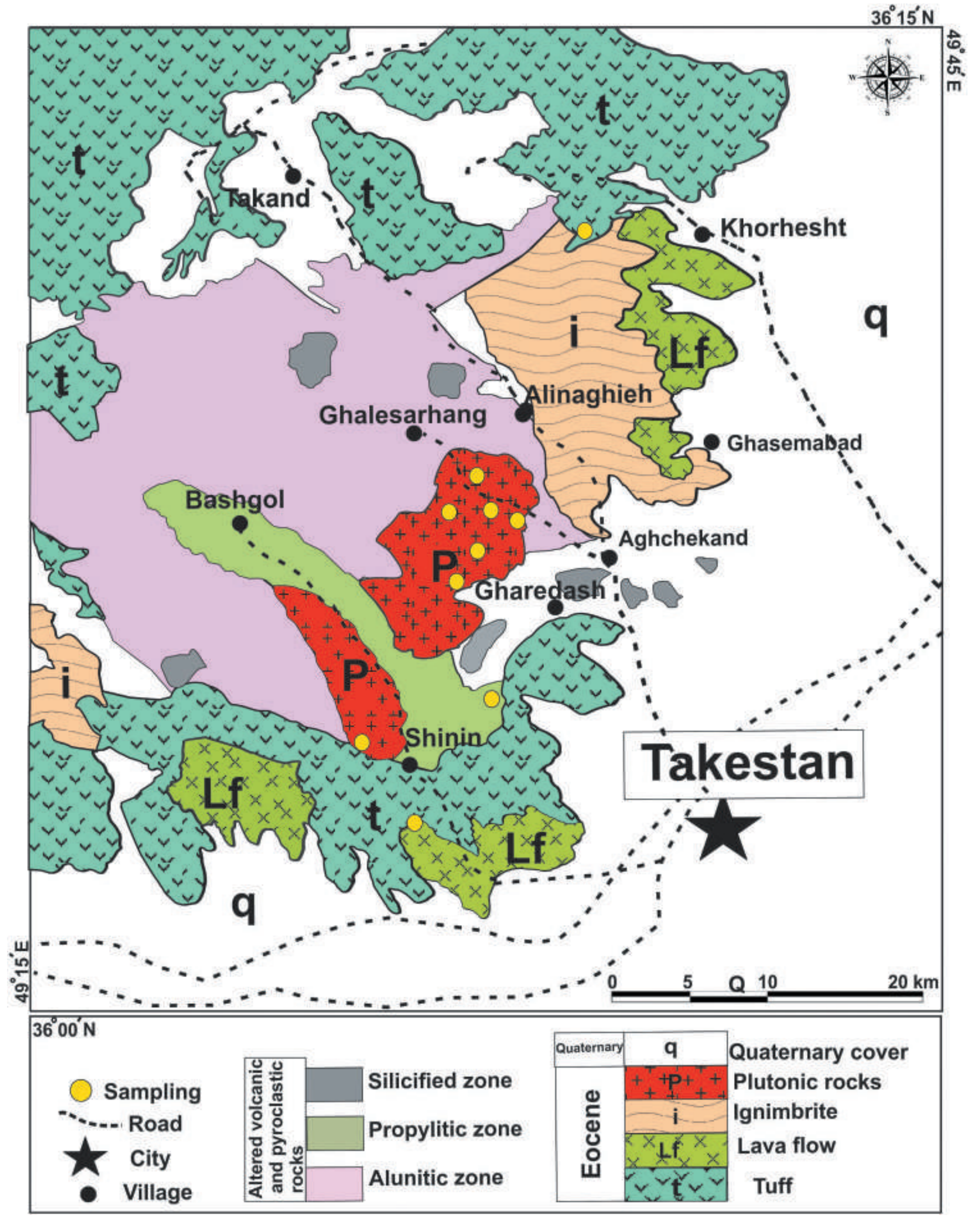

Figure 2. Simplified geological map of the study area (modified after Alai Mahabadi and Fanoudi 1992; 1: 100,000 Takestan geological map).

Berberian *et al.* 1982). The time of the end of this subduction and the collision of the Arabian plate with the Central Iran block is very controversial and interpreted as the Late Cretaceous (Berberian and King 1981), Eocene to Miocene (Rabiee *et al.* 2022), Miocene (Berberian and Berberian 1981; Berberian *et al.* 1982; Sengör *et al.* 1988; Mohajjel *et al.* 2003), Late Oligocene–Miocene (Stern et al. 2021) and the Late Pliocene (Stöcklin 1968). The subduction-related magmatism in Iran occurred first during the Mesozoic but peaked in the early to late Eocene, followed by collisional magmatism in the Early Oligocene (~32 Ma; (Allen and Armstrong 2008)). On the basis of regional stratigraphy and thermochronological data, many researchers consider the initiation of continent–continent collision and uplift is related to compressive tectonics in the Alborz and Kopeh Dagh ranges occurring in the Late Eocene-Early Oligocene (Lyberis and Manby 1999; Allen *et al.* 2003; Allen and Armstrong 2008; Dargahi *et al.* 2010; Hollingsworth *et al.* 2010; Agard *et al.* 2011; Ballato *et al.* 2011; Rezaeian *et al.* 2012; McQuarrie and Van Hinsbergen 2013).

The stratigraphic and structural data from the Alborz range indicate the development and subsequent deformation of late Miocene intermountain basins in the western Alborz (Guest *et al.* 2007). A late Miocene to Pliocene age was suggested for the main shortening phase in the western and central Alborz (Axen *et al.* 2001; Allen *et al.* 2003; Guest et al. 2006, 2007; Ballato et al. 2008, 2011; Rezaeian *et al*. 2012). This tectonic event has been related to Arabia-Eurasia collision and also to the onset of rapid sedimentation and subsidence in the South Caspian Basin (ca. 6 Ma; Nadirov *et al*. 1997), the activation of transpressional deformation resulting in the development of thrusts and folds in the Central Iran basin (Morley *et al*. 2009) and the onset of molasse deposition along the Zagros Ranges (Homke *et al*. 2004).

Asiabanha *et al*. (2009) have divided the sequence of magmatic rocks in western Alborz into three phases: submarine eruptions, aerial eruptions, and plutonism. The first stratigraphic studies and classification of Palaeogene volcanic and intrusive rocks in the western Alborz was performed by Annells *et al*. (1975) in Taleghan and Qazvin regions. They divided the Palaeogene volcanic eruptions into three volcanic phases. Phase 1 (Eocene) in many places is composed of felsic and andesitic tuffs and tuffaceous mudstones, and phase 2 and 3 (Oligocene) are composed of mafic and andesitic to more acidic lava flows, respectively.

In the northwestern region of Takestan (in western Alborz, location 1 in Figure 1), between 49° 15′ and 49° 45′ longitudes and 36° 00′ and 36° 15′ latitudes, a variety of pyroclastic deposits, lava flows, and deeper plutonic and subvolcanic rocks occur (Figure 2). The igneous rocks of this area from oldest to youngest are: the lava flows (andesite, trachyandesite, basaltic andesite, and basalt), the pyroclastic deposits (crystalline and lithic tuff, agglomerate, ignimbrite), the plutonic rocks (monzodiorite, quartz monzonite, granite, alkali granite) and subvolcanic rocks (dacitic and rhyolitic domes).

Methods

About 120 samples of effusive volcanic, pyroclastic, and plutonic rocks were collected in situ from the study area. From these rocks, 56 thin sections were prepared for petrographic studies and 10 polished thin sections for zircon U-Pb dating. These 10 samples were seven plutonic and three volcanic samples; including three alkali feldspar granite samples (MgB4, MgGd1, VN16), two granites (Dgs3, GN3), one quartz monzonite (GN7), one monzodiorite (GN8), two rhyolites (VGd1, VN12), and one dacite sample (KhD5). The U-Pb laser ablation inductively coupled plasma-mass spectrometry (LA ICP-MS) geochronology was conducted at the University New Brunswick in Canada on 30 µm thick polished thin sections following standard procedures (McFarlane and Luo 2012). The target grains were analysed using an Australian Scientific Instruments *M*-50-LR193 nm ArF excimer laser ablation system coupled to Agilent 7700× quadrupole ICP-MS on polished thin-sections. The beam size was 5 micrometres when the laser was in operation. Crater diameter was 30 µm for zircon dating. Data reduction was done using Iolite™ and Vizual Age™. Data output and assessment of accuracy were done using quality-control reference materials (e.g. Plesovice zircon). The age and Hf isotopic homogeneity of the Plesovice zircon together with its relatively high U and Pb contents make it an ideal calibration and reference material for LA ICP-MS measurements, especially when using low laser energies and/or small diameters of laser beam required for improved spatial resolution (Sláma *et al*. 2008). Total analysed spots on zircon grains are 172 including 32 spots for GN8 sample, 13 spots for DgS3 sample, 31 spots for GN7 sample, 8 spots for GN3 sample, 18 spots for MgB4 sample, 14 spots for MgGd1 sample, 15 spots for VN16 sample, 18 spots for VGd1 sample, 7 spots for KhD5 sample, and 16 spots for VN12 sample. Concordia diagrams were drawn by ISOPLOT/EX 3.75 software (Ludwig 2003).

Field geology

The exposed rock units NW of Takestan (from older to younger) include pyroclastic rocks, lava flows, ignimbrites (Figure 3a), and sub-volcanic and plutonic rocks. Pyroclastic rocks are the main rock facies that have spread throughout the region. They comprise various types of submarine and aerial deposits. The phase 1 (submarine eruptions) include crystalline and lithic tuff and agglomerate. The presence of microfossils such as Nummulites sp., Nummulites globules, Discocyclina sella, and Actinocyclina sp. among the pyroclastic layers indicates the formation of these rocks in an Eocene shallow marine basin (Asiabanha *et al*. 2009). Lava flows are included in the subsequent eruption phase (phase 2 or aerial eruptions with approximately 700–800 m thickness). The ignimbrites have the limited outcrops and are underlain by the older tuffs in some places (Figure 3b). The colour of these ignimbrites is mostly pink and grey. According to Cas and Wright (1988), the presence of ignimbrite units can be evidence of the existence of caldera during calc-alkaline magmatic activities. In most cases ignimbrites are related to fissure type vents and graben collapse volcanic structures that have named graben calderas (Aguirre-Díaz *et al*. 2008). Volcanic rocks include basalt, basaltic andesite and andesite. They have a typical porphyritic texture. These rocks include abundant joints filled with secondary minerals, such as quartz and calcite. Subsequently or simultaneously with volcanic rocks, subvolcanic rocks have been injected in the form of dacitic and rhyolitic domes (phase 3) (Figure 3c). In the later stage of magmatic activities resulted in plutonic rocks that intruded tuffs (Figure 3d,e). In some places, dacitic and rhyolitic

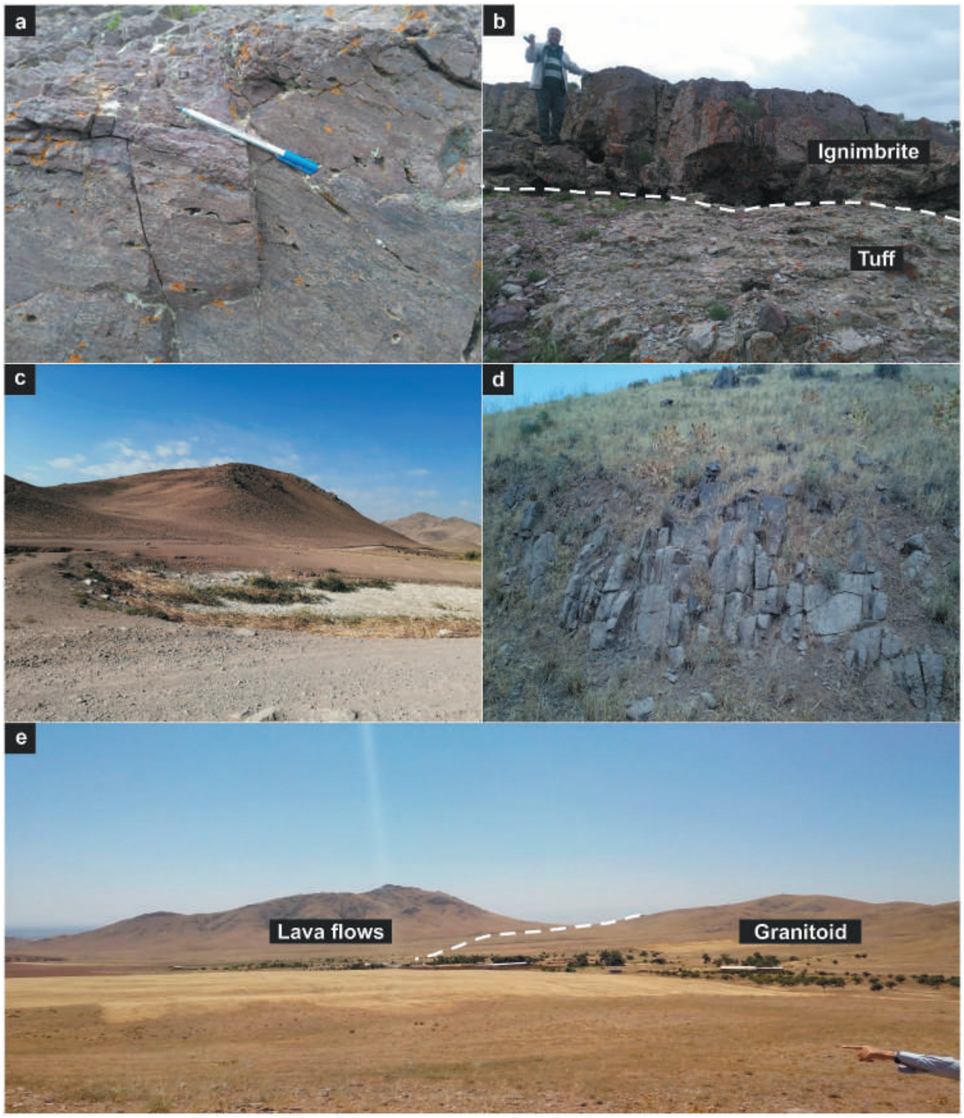

Figure 3. Major outcrops of rock units, (a) ignimbrite; (b) ignimbrite on tuff; (c) rhyolitic dome; (d) granitoid (monzodiorite); (e) lava flows next to the granitoid.

domes have formed around fractures and faults along the caldera collapse. Plutonic rocks include monzodiorite (Figure 3d), quartz monzonite, granite, and alkali feldspar granite. They display a change in lithology (from north to south) so that in the northern parts, the composition is diorite to monzodiorite, in the central parts is quartz monzonite and in the southern parts is alkali feldspar granite.

Petrography

Plutonic rocks

On the basis of modal analyses, the Takestan plutonic rocks are classified as alkali feldspar granite, granite, quartz monzonite, and monzodiorite. Mineralogy is reported in modal percent in the samples.

Alkali feldspar granite

The samples of alkali feldspar granite from this study are leucocratic and fine to medium grained. In hand specimen, they are white grey to pink. In many places in different samples they have subhedral granular texture characterized petrographically, but some have micro-granular and granophyric textures. The volume of alkali feldspar in this rock is 40–50 (modal %), which in some thin sections display perthitic textures. The other common minerals are quartz (20–30%), plagioclase (<10%), biotite (5–10%), and opaque minerals (3–5%). Titanite, apatite, and zircon are key accessory minerals. Quartz crystals are subhedral to anhedral. In thin sections of these rocks, there are significant amounts of zircon grains (5–10 grains or more). Euhedral zircon grains are found within biotite (Figure 4a) or as individual grains in the groundmass. Titanite occurs as both primary magmatic and secondary as a result of alteration of Ti-bearing Fe oxides minerals and biotite. Primary titanite grains are as subhedral crystals, but secondary ones are small anhedral grains associated with altered minerals. Other secondary minerals include sericite and chlorite.

Granite

They are leucocratic and fine to medium grained. In hand-specimen they are white grey to grey. The most important textures of the granites are subhedral granular, granophyric (Figure 4b), and perthitic textures. The common minerals are alkali feldspar (35–40%), plagioclase (20–25%), quartz (10–15%), biotite (10–15%), and

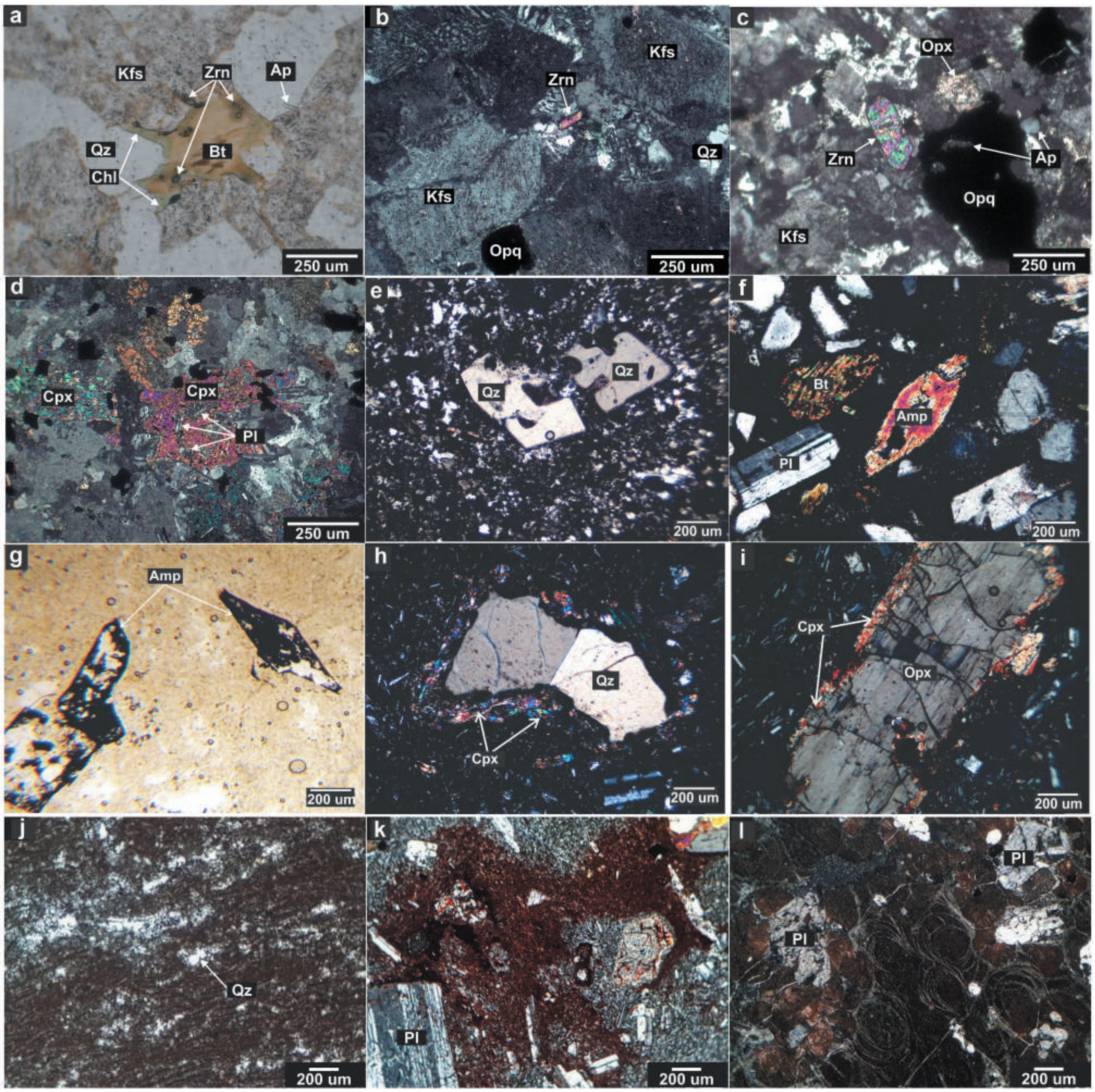

Figure 4. Photomicrographs of the rocks, (a) zircons within biotite in alkali feldspar granite (in PPL); (b) granophyric texture in granite; (c) coarse zircon in quartz monzonite; (d) ophitic and subophitic texture in monzodiorite; (e) vitrophyric texture and embayed quartz grains in rhyolite; (f) vitrophyric and glomeroporphyritic texture in dacite; (g) Opacitic amphibole in andesite and trachyandesite; (h) microlithic porphyritic texture and Ocelli quartz in basaltic andesite; (i) microlithic porphyritic texture and thin layer of fine-grained ca pyroxenes on the margin of orthopyroxene phenocryst; (j) crystal tuff; (k) rock fragments in a hyaloporphyric groundmass in lithic tuff; (l) perlitic texture in ignimbrite. All photomicrographs except (a) and (g) are in XPL (abbreviations of minerals from Whitney and Evans 2010).

opaque minerals (2–4%). The main accessory mineral in these rocks is zircon. Euhedral zircon grains are found as individual grains in the groundmass and some are within biotite. Sericite and chlorite are secondary minerals.

Quartz monzonite

Quartz monzonite is a major part of the Takestan plutonic rocks. These rocks are mesocratic and are grey in hand specimen. The main texture in these rocks is subhedral granular texture. Quartz monzonites are composed of plagioclase (40–50%), alkali feldspar (15–20%), Ca pyroxene (20–25%), quartz (5–10%), biotite (~5%), and opaque minerals (4–5%). Some K-feldspars are perthitic. Some pyroxenes have been altered to secondary minerals such as chlorite and epidote. Accessory minerals include zircon and apatite. The size of zircons is relatively coarse (up to 0.3 mm) in some samples (Figure 4c). Secondary minerals include sericite, biotite, chlorite, and epidote.

Monzodiorite

Monzodiorites are mesocratic to melanocratic and fine to medium grained. In hand specimen they are dark grey. These rocks have subhedral granular texture and some samples have ophitic and sub-ophitic texture (Figure 4d). The common minerals are plagioclase (40–50%), Ca pyroxene (30–40%), alkali feldspar (10–15%), opaque minerals (5–10%) and quartz (<5%). Plagioclase crystals with idiomorphic to sub-idiomorphic shapes and polysynthetic twins are the main leucocratic mineral. Some K-feldspar crystals have perthitic texture. Accessory minerals include zircon and apatite. Secondary minerals are sericite, biotite, chlorite, and epidote.

Volcanic rocks

The volcanic rocks in the Takestan area include rhyolite, dacite, andesite, trachyandesite, basaltic andesite, and basalt.

Rhyolite

The samples of rhyolite in this area are leucocratic. In hand specimen they are light grey with porphyritic texture. In thin sections, the main texture is vitrophyric, although there is also vesicular texture, and some of the vesicles are filled with quartz. The main phenocrysts are quartz, sanidine, biotite, and opaque minerals. Some quartz crystals have an embayed texture (Figure 4e). Accessory minerals include zircon and apatite. Secondary minerals are sericite, calcite, and quartz. Most zircon and apatite grains are present alongside the opaque minerals, but some are seen in the groundmass.

Dacite

In hand specimen these rocks are leucocratic and are grey with porphyry texture. In thin sections, these rocks have vitrophyric texture (Figure 4f). The common phenocrysts are plagioclase, biotite, amphibole, pyroxene, quartz, and opaque minerals. Accessory minerals include zircon and apatite. Some biotite and amphibole minerals are opacitic from margins to cores. Some pyroxene grains have been completely altered and converted to biotite, but the appearance of the crystals indicates that they are Ca pyroxene. Secondary minerals include sericite, calcite, and biotite.

Andesite and trachyandesite

The andesitic and trachyandesitic rocks in hand specimen are mesocratic with porphyritic texture. The most important characteristics of these rocks is vitrophyric texture. Vesicles in some samples are filled with secondary minerals, such as calcite, chlorite, epidote, and quartz. Also, glomeroporphyritic texture is seen in some samples. In andesites and trachyandesites, the common phenocrysts include plagioclase, amphibole, biotite, pyroxene, and opaque minerals. Some plagioclase crystals have sieved texture and some biotite and amphibole minerals have higher opacity (Figure 4g). Secondary minerals include sericite, calcite, quartz, and epidote.

Basaltic andesite and basalt

In hand specimen these rocks are melanocratic with porphyritic texture. They display microlithic porphyritic and trachytic texture (Figure 4h,i). Glomeroporphyritic texture is also evident in some samples. The main phenocrysts include plagioclase, Ca pyroxene, and opaque minerals. Small olivine grains were observed in the groundmass, which often some of them have converted to iddingsite. In some samples quartz xenocrysts are surrounded by fine Ca pyroxene crystals (ocelli quartz) (Figure 4h). Some plagioclase crystals have sieve texture. On the margin of some orthopyroxene phenocrysts, a thin layer of fine-grained, fibrous Ca pyroxenes is present (Figure 4i). Secondary minerals are calcite, chlorite, and iddingsite.

Pyroclastic rocks

These rocks include tuff, agglomerate, and ignimbrite. Tuffs are in the form of crystal tuff and lithic tuff. In crystal tuffs, the groundmass is composed mostly of fine-grained quartz crystals, in which the fragments of plagioclase, quartz, alkali feldspar, amphibole, biotite, and pyroxene can be seen (Figure 4j). In lithic tuffs, rock fragments are placed in a hyaloporphyritic groundmass (Figure 4k). In some of these tuffs, the groundmass has a flow banded and locally spherolitic texture. The flow banding in the microcrystalline groundmass consists mostly of quartz. In the ignimbritic samples, the flow banding results from the differential welding of glass shards. Along with these rock fragments, plagioclase, quartz, and Ca pyroxene crystals is present locally. Some ignimbrites have a perlitic texture (Figure 4l).

Geochronology

Details of determined values, isotopic ratios, and age calculations for the studied samples are reported in the supplementary Tables 1–4. The high Th/U ratios (0.15–3.08) in zircons, are consistent with their magmatic origin (Belousova *et al*. 2002; Kirkland *et al*. 2015). Based on SEM-BSE images most of zircon grains are not zoned (Supplementary Fig. S1).

Samples descriptions and Concordia diagrams

Alkali feldspar granite (samples: MgB4, MgGd1, VN16)

The zircons in these rocks are mostly fine grained (10–100 μm long), transparent, colourless to pale green (Figure 5a,b). They are euhedral to subhedral and represent tabular to prismatic shapes.

On the weight mean diagram for the MgB4 sample (Figure 6a), the weighted mean age is 39.30 ± 0.84 Ma with mean square weighted deviation (MSWD) = 4.5 and a concordance probability of 0.00. The Th/U ratios in its zircons are 0.15–1.82. In MgB4 sample two older zircons with $^{206}Pb/^{238}U$ ages of 43.9 and 46.3 Ma (earlier components) and two zircons with $^{206}Pb/^{238}U$ ages of 56 and 81 Ma (inherited zircons) are present. For the MgGd1 sample, the Concordia diagram (Figure 6b) shows that the weighted mean age is 39.54 ± 0.45 Ma with MSWD = 3.9 and concordance probability of 0.049. The Th/U ratios for the zircons in this sample are 0.23–2.01. In this sample older zircons are also present. Three of them ($^{206}Pb/^{238}U$ ages of 42.6, 42.9, and 43.8 Ma) may represent an earlier component that crystallized in the magma chamber, suggesting slow cooling (Schaltegger *et al*. 1999); One of them ($^{206}Pb/^{238}U$ age of 2340 Ma) represents an inherited zircon from older continental crust. The weighted mean age on the weight mean diagram is 37.46 ± 0.50 Ma for the VN16 sample, (Figure 6c) with MSWD = 0.9 and concordance probability of 0.41. Its zircon Th/U ratios change from 0.17 to 2.37. Eight older zircons with $^{206}Pb/^{238}U$ ages of 40–43 Ma (earlier components) and two zircons with $^{206}Pb/^{238}U$ age of 47.2 and 50.8 Ma (probable inherited zircon) are present.

Granite (samples: Dgs3 and GN3)

Zircon is the key accessory mineral in these rocks. The zircons are mostly medium grained (50–200 μm long), colourless to pale green or pale brown (Figure 4b,c). They are commonly euhedral to subhedral prismatic grains.

For the Dgs3 sample, the Concordia diagram (Figure 6d) shows that the weighted mean age is, 39.28 ± 0.44 Ma with MSWD = 0.055 and concordance probability of 0.81. The Th/U ratios in its zircons are 0.35–1.79. Older zircons are also present both as earlier components in a long-lived magma chamber (five samples with $^{206}Pb/^{238}U$ ages of 42–46 Ma) and inherited zircons from older continental crust ($^{206}Pb/^{238}U$ age of 50.2 Ma). On the Concordia diagram for the GN3 sample (Figure 6e), the weighted mean age is 41.4 ± 2.4 Ma and a concordance probability of 0.00. The Th/U ratios for the zircons in this sample are 0.50–0.97. Three inherited zircons from older continental crust are also present ($^{206}Pb/^{238}U$ age of 52.1, 85.9, and 132 Ma).

Quartz monzonite (sample: GN7)

In quartz monzonite samples the zircons are mostly 50–300 μm in length, colourless to pale green (Figure 5c). They are commonly euhedral to subhedral showing prismatic shapes. For the GN7 sample, the Concordia diagram (Figure 6f) shows that the weighted mean age is, 39.92 ± 0.59 Ma with MSWD = 6.4 and concordance probability of 0.011. The Th/U ratios for the zircons in this sample are 0.4–2.19. Six older zircons with 206Pb/238 U ages of 45–49 Ma represent earlier components and one zircon with $^{206}Pb/^{238}U$ age of 55.8 Ma is probably inherited zircon.

Monzodiorite (sample: GN8)

The zircon grains in this sample are fine-grained (50–100 μm long), colourless to pale brown (Figure 5d). They are commonly euhedral to subhedral with prismatic shapes. The weighted mean age on the Concordia diagram is 39.56 ± 0.49 Ma for the GN8 sample, (Figure 6g) with MSWD = 1.5 and concordance probability of 0.22. Its zircon Th/U ratios are 0.54 to 2.75. Three older zircons with $^{206}Pb/^{238}U$ ages of 43.1, 47.7 and 48 Ma (earlier components) and Four zircons with $^{206}Pb/^{238}U$ age of 50, 53.2, 53.3 and 68.6 Ma (inherited zircon) are present.

Rhyolite (samples: VGd1 and VN12)

In these rocks zircon grains are fine to medium grained (10–200 μm in length), colourless to pale

Table 1. U-Pb LA-ICPMS data of analysed zircon grains in alkali feldspar granite samples from the Takestan area (samples: MgB4, MgGd1, VN16).

	Concentration (ppm)		Measured Isotopic Ratios									Measured Isotopic Ages				
Spot	U	Th	Th/U	$^{207}Pb/^{206}Pb$	2σ	err.	$^{206}Pb/^{238}U$	2σ	err.	$^{207}Pb/^{235}U$	2σ	$^{207}Pb/^{235}U$	2σ	$^{206}Pb/^{238}U$ Age	2σ	Discordancy
mgB4–6	2800	1790	0.639	0.026	0.044	0.37	0.0052	0.0004	0.7343	0.03	0.032	37	32	33.4	2.5	Concordant
mgB4–10	3100	5394	1.74	0.0849	0.005	−0.05	0.0053	0.0002	0.4029	0.064	0.004	62.7	4.1	33.82	1	Discordant
mgB4–1	1057	867	0.82	0.0503	0.006	−0.03	0.0058	0.0002	0.2559	0.041	0.005	40.3	4.9	37.31	1.1	Concordant
mgB4–15	397.7	313	0.787	0.0539	0.007	0.32	0.0058	0.0002	0.0427	0.044	0.006	45.7	5.2	37.5	1.4	Concordant
mgB4–16	3927	2844	0.724	0.0475	0.002	0.12	0.006	0.0001	0.1686	0.04	0.002	39.5	2.1	38.55	0.92	Concordant
mgB4–14	1782	1359	0.763	0.0509	0.003	0.16	0.006	0.0002	0.2309	0.043	0.003	42.5	2.5	38.76	1	Concordant
mgB4–2	103.7	65.5	0.632	0.062	0.018	0.27	0.0062	0.0003	0.018	0.05	0.016	49	15	39.7	2.3	Concordant
mgB4-1-1	5338	4523	0.847	0.0466	0.002	0.03	0.0062	0.0001	0.3679	0.04	0.002	40.1	2	39.88	0.88	Concordant
mgB4–4	110.5	100.4	0.909	0.054	0.019	0.13	0.0062	0.0004	0.2629	0.048	0.016	46	16	40.1	2.8	Concordant
mgB4–3	6480	1219	0.188	0.05	0.026	−0.05	0.0063	0.0003	0.9013	0.042	0.027	45	27	40.2	2.1	Concordant
mgB4–11	4118	620	0.151	0.069	0.004	0.18	0.0063	0.0001	0.0815	0.061	0.004	59.8	3.5	40.48	0.93	Discordant
mgB4-1-2	3270	1010	0.309	0.0481	0.002	0.12	0.0063	0.0001	0.0717	0.042	0.002	41.6	2.2	40.7	0.89	Concordant
mgB4–12	4970	2770	0.557	0.0702	0.003	0.02	0.0068	0.0002	0.5903	0.066	0.004	65.3	3.4	43.9	1.3	Discordant
mgB4–8	4260	1598	0.375	0.695	0.015	−0.77	0.0126	0.002	0.9134	0.13	0.26	170	220	81	13	Discordant
mgB4–5	250.4	302	1.206	0.141	0.018	0.057	0.0072	0.0003	0.4502	0.135	0.018	127	16	46.3	2.2	Discordant
mgB4–9	617	494	0.801	0.276	0.023	0.187	0.0087	0.0003	0.173	0.332	0.03	289	22	56	1.8	Discordant
mgGd1–8	5860	5090	0.869	0.104	0.0052	0.45	0.0061	0.0003	0.7255	−0.007	0.043	8	36	39	2.2	Discordant
mgGd1–2	9490	19137	2.017	0.039	0.017	−0.65	0.0061	0.0002	0.6809	0.033	0.016	32	16	39	1.3	Concordant
mgGd1-5-1	724	613	0.847	0.0479	0.006	0.1	0.0061	0.0002	0.0373	0.04	0.005	40.6	5.1	39.02	1.2	Concordant
mgGd1–7	3796	1572	0.414	0.0481	0.0025	0.28	0.0061	0.0001	0.0477	0.04	0.002	40.3	2.3	39.36	0.9	Concordant
mgGd1-5-2	878	704	0.802	0.0482	0.0053	0.38	0.0061	0.0002	0.1348	0.042	0.004	41.4	4.2	39.5	1.3	Concordant
mgGd1–4	1704	2304	1.352	0.0493	0.0026	0.22	0.0062	0.0001	0.0614	0.042	0.003	41.9	2.5	39.93	0.97	Concordant
mgGd1–1	3750	880	0.235	0.0533	0.005	0.55	0.0063	0.0002	0.3306	0.045	0.004	46.2	4.4	40.76	1.2	Concordant
mgGd1-10-2	231	100.5	0.435	0.058	0.011	0.33	0.0068	0.0003	0.0719	0.052	0.009	51.4	8.9	43.8	2.3	Concordant
mgGd1-10-1	95.3	78.2	0.821	0.048	0.021	0.1	0.0066	0.0005	0.1628	0.054	0.018	51	17	42.6	3.5	Concordant
mgGd1-10-4	75.6	74.8	0.989	0.096	0.042	0.8	0.0059	0.0004	0.1507	0.055	0.021	50	20	37.8	2.6	Concordant
mgGd1–3	1530	1204	0.787	0.075	0.0098	−0.55	0.0062	0.0002	0.7376	0.063	0.009	61.8	8.8	39.8	1.5	Discordant
mgGd1–6	844	744	0.882	0.0705	0.009	0.14	0.0067	0.0002	0.1149	0.067	0.009	65.4	8.3	42.9	1.6	Discordant
mgGd1-10-3	105.5	120.8	1.145	0.11	0.025	0.25	0.0063	0.0004	0.2024	0.087	0.02	82	17	40.6	2.4	Discordant
mgGd1–9	1980	3640	1.838	0.6	0.1	−0.6	0.64	0.25	0.875	84	32	2730	610	2340	810	Discordant
VN16–1	6450	1332	0.207	0.059	0.02	−0.87	0.0065	0.0002	0.8307	0.06	0.018	57	17	41.5	1.2	Discordant
VN16–2	8590	4246	0.494	0.052	0.002	0.28	0.0059	0.0001	0.0282	0.042	0.002	41.6	1.7	37.74	0.66	Concordant
VN16–3	8380	7406	0.884	0.055	0.015	−0.86	0.006	0.0001	0.7848	0.041	0.012	44	13	38.66	0.91	Concordant
VN16–4	544	684	1.257	0.062	0.007	0.05	0.0066	0.0002	0.1991	0.056	0.006	54.7	6.1	42.6	1.2	Concordant
VN16–5	1830	1280	0.699	0.069	0.004	0.16	0.0067	0.0002	0.266	0.063	0.004	62.5	3.4	43.12	1.1	Discordant
VN16–6	1590	559	0.352	0.054	0.004	0.32	0.0064	0.0002	0.0967	0.046	0.004	45.9	3.5	40.8	1.3	Concordant
VN16–7	1228	664	0.541	0.155	0.016	−0.55	0.0079	0.0003	0.6818	0.179	0.024	160	19	50.8	2	Discordant
VN16–8	562	525	0.934	0.049	0.005	0.06	0.0058	0.0001	0.2987	0.04	0.004	39.3	3.8	37.02	0.98	Concordant
VN16–9	236.6	291	1.23	0.045	0.011	0.08	0.0058	0.0002	0.0064	0.037	0.009	36.4	8.5	37.1	1.4	Concordant
VN16–10	1234	218	0.177	0.046	0.005	0.13	0.0051	0.0001	0.1296	0.032	0.003	31.8	2.9	32.71	0.83	Concordant
VN16–11	55.2	47.1	0.853	0.203	0.042	0.27	0.0074	0.0006	0.0754	0.225	0.044	193	37	47.2	3.7	Discordant
VN16–12	1447	1005	0.695	0.05	0.005	0.06	0.0062	0.0002	0.0369	0.043	0.004	43.2	3.6	40	1.2	Concordant
VN16–13	259	176.8	0.683	0.058	0.01	0.35	0.0064	0.0003	0.0148	0.051	0.008	51.3	7.8	41.1	1.9	Concordant
VN16–14	5670	13491	2.379	0.06	0.021	−0.77	0.0064	0.0002	0.7908	0.059	0.019	58	19	41.3	1.2	Discordant
VN16–15	345.1	290	0.84	0.081	0.009	0.39	0.0063	0.0002	0.1539	0.07	0.008	68.3	7.3	40.1	1.3	Discordant

Table 2. U-Pb LA-ICPMS data of analysed zircon grains in granite samples from the Takestan area (samples: DgS3, GN3).

	Concentration (ppm)			Measured Isotopic Ratios								Measured Isotopic Ages				
Spot	U	Th	Th/U	$^{207}Pb/^{206}Pb$	2σ	err.	$^{206}Pb/^{238}U$	2σ	err.	$^{207}Pb/^{235}U$	2σ	$^{207}Pb/^{235}U$	2σ	$^{206}Pb/^{238}U$ Age	2σ	Discordancy
DgS3–13	4220	4780	1.133	0.019	0.031	−0.31	0.006	0.00037	0.925	0.02	0.03	24	31	38.6	2.4	Discordant
DgS3–2	3313	2750	0.83	0.008	0.054	−0.94	0.006	0.00038	0.951	0.026	0.04	32	41	38.5	2.4	Concordant
DgS3–7	824.6	1062	1.288	0.0457	0.005	0.09	0.0061	0.00016	0.184	0.0379	0.004	37.6	3.9	39.25	1	Concordant
DgS3–6	766	450	0.587	0.0468	0.004	0.12	0.006	0.00017	0.078	0.038	0.004	37.7	3.6	38.33	1.1	Concordant
DgS3–5	820	312	0.38	0.053	0.005	0.085	0.0061	0.00018	0.091	0.0431	0.004	42.7	3.9	39.07	1.1	Concordant
DgS3–9	299	107.1	0.358	0.063	0.011	0.023	0.0061	0.00036	0.246	0.0526	0.01	51.6	9.2	39.4	2.3	Concordant
DgS3–3	177.7	216.3	1.217	0.088	0.02	−0.16	0.0066	0.00037	0.412	0.082	0.021	77	19	42.4	2.3	Discordant
DgS3–8	371.3	315.3	0.849	0.107	0.014	0.09	0.0062	0.00026	0.274	0.089	0.013	87	12	39.9	1.7	Discordant
DgS3–12	889	530	0.596	0.116	0.016	−0.2	0.0069	0.00024	0.436	0.106	0.016	101	14	44	1.5	Discordant
DgS3–11	5030	9031	1.795	0.114	0.011	−0.36	0.0072	0.00026	0.505	0.114	0.013	109	11	46.5	1.7	Discordant
DgS3–10	4840	4530	0.936	0.126	0.011	−0.36	0.0069	0.00022	0.551	0.123	0.013	117	12	44.4	1.4	Discordant
DgS3–4	150.6	171	1.135	0.128	0.024	0.08	0.0067	0.00034	0.256	0.127	0.024	119	22	42.9	2.2	Discordant
DgS3–1	447	261	0.584	0.171	0.03	−0.02	0.0078	0.00036	0.125	0.208	0.046	181	36	50.2	2.3	Discordant
GN3–3	115.9	107.7	0.929	0.06	0.014	−0.11	0.0063	0.00037	0.152	0.045	0.011	43	11	40.4	2.4	Concordant
GN3–5	83.9	67.2	0.801	0.044	0.021	0.09	0.0065	0.00048	0.001	0.045	0.02	44	19	41.9	3.1	Concordant
GN3–8	111.3	107.8	0.969	0.074	0.02	0.23	0.0063	0.00042	0.065	0.062	0.016	58	15	40.9	2.7	Concordant
GN3–2	78.1	55.3	0.708	0.09	0.027	0.37	0.0066	0.00053	0.018	0.07	0.019	65	18	42.3	3.4	Discordant
GN3–6	88.2	79.4	0.9	0.073	0.021	0.06	0.0065	0.00039	0.226	0.07	0.019	65	18	41.6	2.5	Discordant
GN3–1	96.1	48.8	0.508	0.16	0.036	0.45	0.0081	0.00062	0.101	0.185	0.04	169	33	52.1	3.9	Discordant
GN3–4	52	36	0.692	0.462	0.045	0.27	0.0134	0.0009	0.453	0.789	0.09	587	49	85.9	5.7	Discordant
GN3–7	10744	6850	0.638	0.317	0.039	−0.61	0.0208	0.0026	0.918	1.15	0.23	661	98	132	17	Discordant

Table 3. U-Pb LA-ICPMS data of analysed zircon in quartz monzonite and monzodiorite samples grains from the Takestan area (samples: GN7, GN8).

	Concentration (ppm)		Measured Isotopic Ratios									Measured Isotopic Ages				
Spot	U	Th	Th/U	$^{207}Pb/^{206}Pb$	2σ	err.	$^{206}Pb/^{238}U$	2σ	err.	$^{207}Pb/^{235}U$	2σ	$^{207}Pb/^{235}U$	2σ	$^{206}Pb/^{238}U$ Age	2σ	Discordancy
GN7-19- 1	406	395.5	0.974	0.0743	0.01	0.28	0.0065	0.0003	0.1389	0.0664	0.009	66.2	8.5	41.5	1.8	Discordant
GN7-19- 2	356	212	0.596	0.071	0.009	0.46	0.0073	0.0003	0.2015	0.0692	0.008	69.8	7.8	46.6	1.8	Discordant
GN7-18-1	142.7	280	1.962	0.039	0.012	0.24	0.007	0.0003	0.1626	0.041	0.012	39	11	45.1	1.9	Concordant
GN7-18-2	672	445	0.662	0.234	0.02	−0.53	0.0087	0.0004	0.8112	0.29	0.036	260	28	55.8	2.6	Discordant
GN7-17-1	4700	3214	0.684	0.07	0.03	−0.85	0.0071	0.0003	0.8527	0.078	0.028	71	27	45.9	1.6	Concordant
GN7-16-1	324.6	301.9	0.93	0.0418	0.007	0.18	0.0064	0.0002	0.0031	0.038	0.007	37.4	6.4	41.3	1.4	Concordant
GN7-15-1	619	547	0.884	0.0476	0.006	0.24	0.0061	0.0002	0.0164	0.0378	0.005	38	4.6	39.42	1.1	Concordant
GN7-14-1	450.2	571	1.268	0.057	0.012	0.15	0.0062	0.0002	0.0824	0.0464	0.009	45.7	8.7	39.5	1.5	Concordant
GN7-13-1	415	327	0.788	0.0479	0.007	0.31	0.0064	0.0002	0.1039	0.0423	0.006	42.5	5.4	41.1	1.3	Concordant
GN7-12-1	515.3	640	1.242	0.057	0.012	0.17	0.0062	0.0003	0.0585	0.0478	0.01	47	9.3	39.5	1.8	Concordant
GN7-12-2	717	280	0.391	0.0506	0.0057	0.17	0.0062	0.0002	0.0988	0.0435	0.005	43	4.8	40	1.3	Discordant
GN7-12-3	601	348	0.579	0.0771	0.007	0.12	0.0064	0.0002	0.1977	0.0659	0.006	65.1	5.6	41.2	1.4	Discordant
GN7-11-1	546	219	0.401	0.0785	0.008	0.42	0.0066	0.0004	0.0305	0.0728	0.007	71.1	6.9	42.6	2.5	Concordant
GN7-11-2	509	336	0.66	0.0568	0.007	−0.03	0.0062	0.0002	0.425	0.0489	0.006	48.2	6.1	39.8	1.5	Concordant
GN7-11-3	729	712	0.977	0.0518	0.005	0.08	0.0063	0.0002	0.1443	0.0453	0.005	44.7	4.4	40.76	1.1	Concordant
GN7-11-4	1000	2190	2.19	0.0575	0.006	0.14	0.0069	0.0003	0.2587	0.0541	0.006	53.4	5.3	44.2	2.1	Discordant
GN7-10-1	251	368	1.466	0.075	0.016	0.28	0.0065	0.0004	0.1086	0.063	0.013	62	13	41.7	2.4	Concordant
GN7-10-2	451	542	1.202	0.0511	0.009	0.21	0.006	0.0002	0.0549	0.0402	0.007	40.6	6.6	38.5	1.4	Discordant
GN7-9-1	528	883	1.672	0.129	0.014	−0.04	0.0062	0.0002	0.1654	0.104	0.011	99.8	9.6	40.1	1.5	Concordant
GN7-9-2	404	421	1.042	0.0648	0.009	0.23	0.0066	0.0003	0.0725	0.0565	0.007	55.3	6.4	42.1	1.6	Discordant
GN7-8-1	216	223.2	1.033	0.076	0.012	0.05	0.0063	0.0003	0.146	0.066	0.011	64	10	40.5	1.8	Discordant
GN7-8-2	176.1	262.2	1.489	0.124	0.021	0.08	0.0065	0.0004	0.2765	0.116	0.022	110	20	41.9	2.7	Discordant
GN7-8-3	141.4	131.1	0.927	0.192	0.036	0	0.0077	0.0007	0.3151	0.187	0.033	170	28	49.2	4.5	Concordant
GN7-7-1	211.3	316.8	1.499	0.043	0.013	0.08	0.0061	0.0003	0.0788	0.035	0.0096	34.3	9.3	38.9	1.8	Discordant
GN7-6-1	1300	2460	1.892	0.0991	0.01	0.01	0.0067	0.0002	0.2952	0.095	0.01	91.6	9.4	43.1	1.4	Concordant
GN7-5-1	622	1043	1.677	0.0488	0.008	0.11	0.0061	0.0002	0.1136	0.0409	0.006	40.5	5.9	39.3	1.3	Discordant
GN7-4-1	3430	4020	1.172	0.097	0.011	−0.19	0.0058	0.0001	0.2009	0.0793	0.01	76.6	8	37.44	0.77	Concordant
GN7-2-1	178	228.6	1.284	0.053	0.013	0.18	0.007	0.0004	0.143	0.052	0.012	47.6	9.9	45.2	2.6	Discordant
GN7-2-2	404	300	0.743	0.073	0.012	−0.23	0.0064	0.0002	0.3049	0.0602	0.0097	58.4	9	41.4	1.5	Discordant
GN7-2-3	276	204.7	0.742	0.109	0.016	0.15	0.0067	0.0002	0.0076	0.098	0.013	91	11	42.8	1.4	Discordant
GN7-1-2	350.7	356	1.015	0.137	0.023	0.06	0.0075	0.0003	0.186	0.144	0.024	134	21	47.8	1.8	Discordant
Gn8–1	2942	2169	0.737	0.065	0.003	−0.01	0.0059	0.0001	0.2358	0.053	0.0025	52.1	2.4	37.71	0.63	Discordant
Gn8-2-1	612	426	0.696	0.043	0.004	0.15	0.0063	0.0002	0.0822	0.037	0.0036	37.5	3.4	40.58	1.1	Concordant
Gn8–3	7840	21611	2.757	0.062	0.002	0.22	0.0057	0.0001	0.4682	0.048	0.002	47.3	1.9	36.74	0.81	Concordant
Gn8–4	370	375	1.014	0.22	0.019	0.07	0.0074	0.0004	0.3219	0.217	0.02	197	17	47.7	2.5	Discordant
Gn8–6	398	372.5	0.936	0.16	0.01	0.37	0.0067	0.0002	0.194	0.144	0.0087	135.5	7.7	43.1	1.3	Discordant
Gn8–7	390	514	1.318	0.045	0.008	0.32	0.0061	0.0002	0.1001	0.039	0.007	38.5	6.9	39.1	1.6	Concordant
Gn8–8	199	229.6	1.154	0.268	0.045	−0.05	0.0083	0.0007	0.4749	0.318	0.059	269	45	53.3	4.6	Discordant
Gn8–10	449	243.1	0.541	0.052	0.005	0.06	0.0059	0.0002	0.1921	0.043	0.0047	42.4	4.5	38.2	1.2	Concordant
Gn8–11	475.9	495	1.04	0.106	0.017	−0.34	0.0067	0.0002	0.5625	0.101	0.019	94	16	42.8	1.6	Discordant
Gn8–12	292	326	1.116	0.059	0.01	0.44	0.0061	0.0003	0.2212	0.05	0.0081	50	7.6	39.3	1.6	Concordant
Gn8–13	323	396	1.226	0.056	0.009	0.28	0.006	0.0002	0.2094	0.045	0.0067	44.4	6.5	38.52	1.1	Concordant
Gn8–14	118.3	269.2	2.276	0.413	0.034	0.29	0.0107	0.0006	0.1836	0.611	0.051	469	31	68.6	3.6	Discordant
Gn8–15	262.2	308.6	1.177	0.052	0.01	−0.18	0.0061	0.0002	0.2942	0.043	0.0079	42	7.6	39.4	1.4	Discordant
Gn8–16	453	389	0.859	0.116	0.01	0	0.0066	0.0002	0.2781	0.104	0.0091	99.6	8.3	42.4	1.3	Concordant
Gn8–17	220.5	141.6	0.642	0.057	0.01	0.34	0.0066	0.0003	0.1445	0.048	0.0074	46.6	7.2	42.1	1.9	Discordant
Gn8–18	435.2	277.8	0.638	0.137	0.012	0.15	0.0067	0.0002	0.1968	0.124	0.011	117.5	9.6	42.8	1.4	Concordant

(*Continued*)

Table 3. (Continued).

	Concentration (ppm)			Measured Isotopic Ratios								Measured Isotopic Ages				
Spot	U	Th	Th/U	$^{207}Pb/^{206}Pb$	2σ	err.	$^{206}Pb/^{238}U$	2σ	err.	$^{207}Pb/^{235}U$	2σ	$^{207}Pb/^{235}U$	2σ	$^{206}Pb/^{238}U$ Age	2σ	Discordancy
Gn8–19	197.6	280.8	1.421	0.078	0.022	0.01	0.0062	0.0003	0.0131	0.065	0.019	55	11	39.6	1.7	Discordant
Gn8–20	318.4	345	1.084	0.242	0.025	−0.41	0.0083	0.0004	0.6464	0.282	0.033	247	27	53.2	2.3	Concordant
Gn8–21	283.4	320.6	1.131	0.159	0.04	−0.08	0.0066	0.0003	0.1482	0.131	0.026	114	13	42.3	1.6	Discordant
Gn8–22	364.7	483.8	1.327	0.219	0.025	0.31	0.0075	0.0004	0.1603	0.223	0.025	211	21	48	2.5	Discordant
Gn8–23	398.9	261.5	0.656	0.057	0.006	0.29	0.0063	0.0002	0.0286	0.049	0.0053	48.3	5.1	40.4	1	Discordant
Gn8–24	495	449	0.907	0.053	0.005	0.34	0.0063	0.0002	0.1022	0.046	0.0039	45.9	3.8	40.7	1.1	Concordant
Gn8–25	467	298	0.638	0.06	0.009	0.06	0.0063	0.0003	0.2801	0.051	0.0076	50.1	7.3	40.7	1.9	Concordant
Gn8–26	717	312	0.435	0.059	0.006	0.09	0.0057	0.0002	0.1713	0.047	0.0049	45.9	4.7	36.87	0.98	Concordant
Gn8–27	169.7	268.2	1.58	0.067	0.015	0.04	0.0064	0.0003	0.07	0.059	0.013	57	13	41.1	2	Concordant
Gn8–28	316.5	311.8	0.985	0.048	0.007	0.07	0.0063	0.0002	0.1546	0.041	0.0059	41.9	6	40.4	1.4	Concordant
Gn8–29	455.7	966	2.12	0.042	0.006	0.22	0.0063	0.0002	0.0209	0.036	0.0048	36	4.7	40.5	1.2	Concordant
Gn8–30	532.4	908	1.705	0.05	0.007	0.14	0.0062	0.0002	0.0898	0.044	0.0058	43.5	5.7	40	1.2	Concordant
Gn8–31	332.9	302.9	0.91	0.221	0.038	−0.65	0.0078	0.0005	0.8115	0.265	0.056	229	45	50	3.5	Concordant
Gn8–32	279.2	267	0.956	0.048	0.008	0.23	0.0061	0.0002	0.0218	0.041	0.0065	40.1	6.3	39.4	1.6	Discordant
Gn8–33	308.9	370	1.198	0.057	0.008	0.24	0.0062	0.0002	0.0626	0.05	0.0066	48.5	6.3	39.8	1.3	Concordant
Gn8–34	177.9	136.8	0.769	0.106	0.018	0.47	0.0064	0.0003	0.2083	0.09	0.013	87	12	40.9	1.7	Concordant

Table 4. U-Pb LA-ICPMS data of analysed zircon grains in rhyolite and dacite samples from the Takestan area (samples: VGd1, VN12, KhD5).

	Concentration (ppm)		Measured Isotopic Ratios									Measured Isotopic Ages				
Spot	U	Th	Th/U	$^{207}Pb/^{206}Pb$	2σ	err.	$^{206}Pb/^{238}U$	2σ	err.	$^{207}Pb/^{235}U$	2σ	$^{207}Pb/^{235}U$	2σ	$^{206}Pb/^{238}U$ Age	2σ	Discordancy
VGd-1–1	347	316	0.911	0.114	0.015	−0.12	0.007	0.0002	0.46	0.107	0.015	101	13	41.9	1.4	Discordant
VGd-1–2	416	318	0.764	0.067	0.008	0.2	0.006	0.0002	0.025	0.054	0.007	52.9	6.5	36.8	1.3	Discordant
VGd-1–3	2870	5270	1.836	0.045	0.003	0.57	0.006	0.0001	0.355	0.035	0.002	35.3	1.8	35.79	0.65	Discordant
VGd-1–4	219	169.5	0.774	0.039	0.009	0.08	0.006	0.0002	0.097	0.03	0.007	29.1	6.7	38.5	1.4	Discordant
VGd-1–5	692	773	1.117	0.051	0.005	0.33	0.006	0.0002	0.019	0.04	0.003	39.2	3.2	37.34	1	Discordant
VGd-1–6	488.1	416.4	0.853	0.05	0.005	0.1	0.006	0.0002	0.172	0.042	0.005	41.1	4.4	38.01	1	Concordant
VGd-1–7	372.6	239.8	0.644	0.054	0.008	0.41	0.006	0.0002	0.107	0.043	0.006	42.5	5.6	37.5	1.2	Concordant
VGd-1–8	1463	2150	1.47	0.047	0.004	0.14	0.006	0.0001	0.077	0.039	0.003	38.9	3	37.29	0.88	Concordant
VGd-1–9	7540	14690	1.948	0.108	0.008	−0.34	0.005	0.0002	0.794	0.038	0.017	36	17	34	1.4	Concordant
VGd-1–10	1332	1655	1.242	0.083	0.007	−0.01	0.005	0.0001	0.269	0.06	0.006	59.1	5.3	34.49	0.84	Concordant
VGd-1–11	2298	4020	1.749	0.049	0.003	0.26	0.006	0.0001	0.021	0.039	0.002	38.6	2.3	36.92	0.75	Concordant
VGd-1–12	3600	8910	2.475	0.047	0.002	−0.12	0.006	0.0001	0.532	0.037	0.002	36.7	1.8	36.13	0.6	Concordant
VGd-1–13	778	996	1.28	0.048	0.004	0.4	0.006	0.0002	0.118	0.038	0.003	37.9	3	37.25	0.96	Concordant
VGd-1–14	606	545	0.899	0.336	0.034	−0.67	0.011	0.0007	0.815	0.557	0.067	438	47	70.6	4.4	Concordant
VGd-1–15	2790	8600	3.082	0.052	0.003	0.17	0.006	0.0001	0.213	0.039	0.002	39.1	2	36.18	0.78	Concordant
VGd-1–16	611	570	0.933	0.062	0.009	0.29	0.006	0.0003	0.063	0.05	0.006	49.5	6.1	38.5	1.7	Concordant
VGd-1–17	458.2	220.9	0.482	0.119	0.013	0.31	0.006	0.0002	0.068	0.108	0.012	103	11	41.6	1.5	Concordant
VGd-1–18	520	330.8	0.636	0.047	0.007	0.26	0.006	0.0002	0.07	0.039	0.006	38.4	5.4	37.7	1.2	Concordant
VN12–8	300.3	167.8	0.559	0.037	0.007	0.04	0.005	0.0002	0.144	0.029	0.006	28.7	5.5	34.6	1.3	Concordant
VN12–14	235.4	175.2	0.744	0.044	0.011	0.37	0.006	0.0003	0.063	0.033	0.008	32.6	7.6	35.7	1.7	Concordant
VN12–13	222.2	250	1.125	0.047	0.011	0.01	0.005	0.0003	0.219	0.035	0.008	33.9	7.5	35.3	1.9	Concordant
VN12–1	380.4	257.9	0.678	0.047	0.008	0.26	0.006	0.0002	0.05	0.037	0.006	36.7	5.8	35.6	1.4	Concordant
VN12–11	459	338.9	0.738	0.048	0.008	0.22	0.005	0.0002	0.15	0.037	0.006	36.8	5.8	35.1	1.4	Concordant
VN12–7	468	441	0.942	0.051	0.009	0.42	0.005	0.0002	0.156	0.038	0.007	37.7	6.4	33.6	1.4	Concordant
VN12–10	619	696	1.124	0.054	0.009	0.15	0.005	0.0002	0.042	0.042	0.007	41.4	6.5	35.3	1.4	Concordant
VN12–15	203.3	124.8	0.614	0.06	0.016	0.1	0.006	0.0004	0.118	0.045	0.012	45	12	35.5	2.4	Concordant
VN12–5	1262	2390	1.894	0.071	0.007	0.12	0.006	0.0002	0.082	0.056	0.005	55.3	5	36.98	1.1	Discordant
VN12–4	1150	2115	1.839	0.129	0.012	0.31	0.006	0.0002	0.091	0.114	0.011	109	9.6	40.2	1.5	Discordant
VN12–3	357.3	439	1.229	0.228	0.032	−0.22	0.007	0.0004	0.579	0.222	0.035	201	27	47.3	2.8	Discordant
VN12–16	374.8	581	1.55	0.246	0.025	−0.32	0.007	0.0003	0.746	0.236	0.028	209	23	46.5	2.1	Discordant
VN12–9	506.1	423.8	0.837	0.265	0.022	0.66	0.007	0.0004	0.248	0.257	0.021	231	17	43.2	2.3	Discordant
VN12–12	337.5	502	1.487	0.465	0.021	0.03	0.011	0.0005	0.708	0.69	0.047	526	28	69.5	3.1	Discordant
VN12–2	383.6	381	0.993	0.719	0.058	0.45	0.024	0.0017	0.482	2.36	0.22	1218	66	150	11	Discordant
VN12–6	205.6	137	0.666	0.829	0.013	0.24	0.224	0.017	0.902	12.1	2.6	2570	190	1293	89	Discordant
KhD5–2	367	412	1.123	0.049	0.009	0.22	0.005	0.0002	0.15	0.037	0.006	36.3	6.1	34.7	1.4	Concordant
KhD5–3	746	578	0.775	0.051	0.006	0.14	0.006	0.0002	0.11	0.043	0.006	42.3	5.5	40.1	1.6	Concordant
KhD5–4	238.5	220.8	0.926	0.059	0.01	0.32	0.006	0.0003	0.004	0.047	0.008	46.2	7.9	38.5	1.7	Concordant
KhD5-3-2	182.4	115.1	0.631	0.061	0.012	0.07	0.006	0.0002	0.069	0.05	0.01	49.4	9.5	38.5	1.5	Discordant
KhD5-3-1	225.1	160.2	0.712	0.063	0.01	0.21	0.006	0.0002	0.084	0.051	0.008	49.5	7.3	38.3	1.5	Discordant
KhD5–1	169.3	125.5	0.741	0.067	0.02	−0.06	0.006	0.0004	0.229	0.055	0.016	53	16	39.2	2.3	Discordant
KhD5–5	145.4	105.8	0.728	0.154	0.019	0.31	0.006	0.0003	0.232	0.126	0.018	120	15	41.5	2.2	Discordant

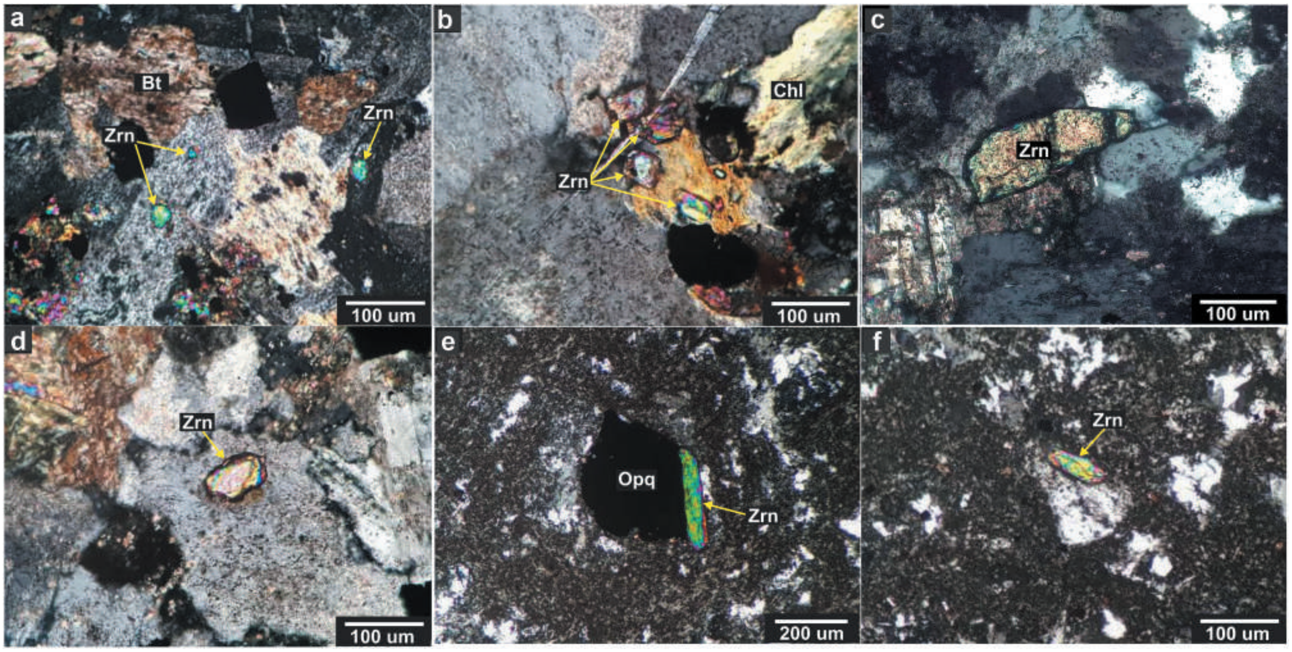

Figure 5. (a) zircon grains in MgB4 sample (alkali granite); (b) zircon grains in VN16 sample (alkali granite); (c) zircon grain in GN7 sample (quartz monzonite); (d) zircon grain in (A) GN8 sample (monzodiorite); (e) zircon grain in Vgd1 sample (rhyolite); (f) zircon grain in KhD5 sample (dacite). All photomicrographs are taken in XPL.

brown. They are mostly euhedral to subhedral with prismatic shapes. Most zircon and apatite are present alongside the opaque minerals (Figure 5e). On the Concordia diagram for the VGd1 sample, (Figure 7a), the weighted mean age is 37.45 ± 0.36 Ma with MSWD = 7.4 and a concordance probability of 0.007. The Th/U ratios for the zircons in this sample are 0.48–3.08. Two older zircons are also present both as earlier components in a long-lived magma chamber ($^{206}Pb/^{238}U$ ages of 41.6 and 41.9 Ma) and one inherited zircon may be from an older continental crust source ($^{206}Pb/^{238}U$ age of 70.6 Ma). For the VN12 sample, the Concordia diagram (Figure 7b) shows that the weighted mean age is, 35.02 ± 0.53 Ma with MSWD = 0.68 and concordance probability of 0.41. The Th/U ratios for the zircons in this sample are 0.55–1.89. Three older zircons with $^{206}Pb/^{238}U$ ages of 43.2, 46.5, and 47.3 Ma (earlier components) and three zircons with $^{206}Pb/^{238}U$ age of 69.5, 150, 1293 Ma (inherited zircon) are present.

Dacite (sample: KhD5)

In this sample zircons are fine-grained (10–100 μm long), colourless to pale brown (Figure 5f). They are usually euhedral to subhedral with prismatic appearance. The weighted mean age on the Concordia diagram is 39.08 ± 1.40 Ma for the KhD5 sample, (Figure 7c) Its zircon Th/U ratios range from 0.63 to 1.12.

Geochronological and geodynamic review of Paleogene magmatism of Iran

Numerous geochronological studies for Alborz Cenozoic magmatic rocks have been performed by various researchers (e.g. Jahangiri 2007; Castro *et al*. 2013; Chiu *et al*. 2013; Nabatian *et al*. 2014; Hasanpour *et al*. 2015; Rabiee *et al*. 2019, 2020); Also, a lot of geochronological studies for Cenozoic magmatic rocks of the other parts of Iran have been conducted (e.g. Dargahi *et al*. 2010 Mazhari *et al*.; Mazhari *et al*. 2011; Honarmand *et al*. 2013; Jamshidibadr and Hassanpour 2015; Omidianfar *et al*. 2018; Azizi *et al*. 2018; Ahmadi *et al*. 2021; Rezaei *et al*. 2021).

Palaeogene magmatic rocks (especially volcanic rocks) are mostly exposed in three main areas in Iran including: The Urumieh-Dokhtar magmatic arc (UDMA), the Lesser Caucasus/Alborz Belt and the Lut block of eastern Iran (e.g. Jung *et al*. 1984) (Figure 1). Also, recent studies indicated that in other parts of Iran such as Sanandaj – Sirjan Zone (SSZ), some magmatic

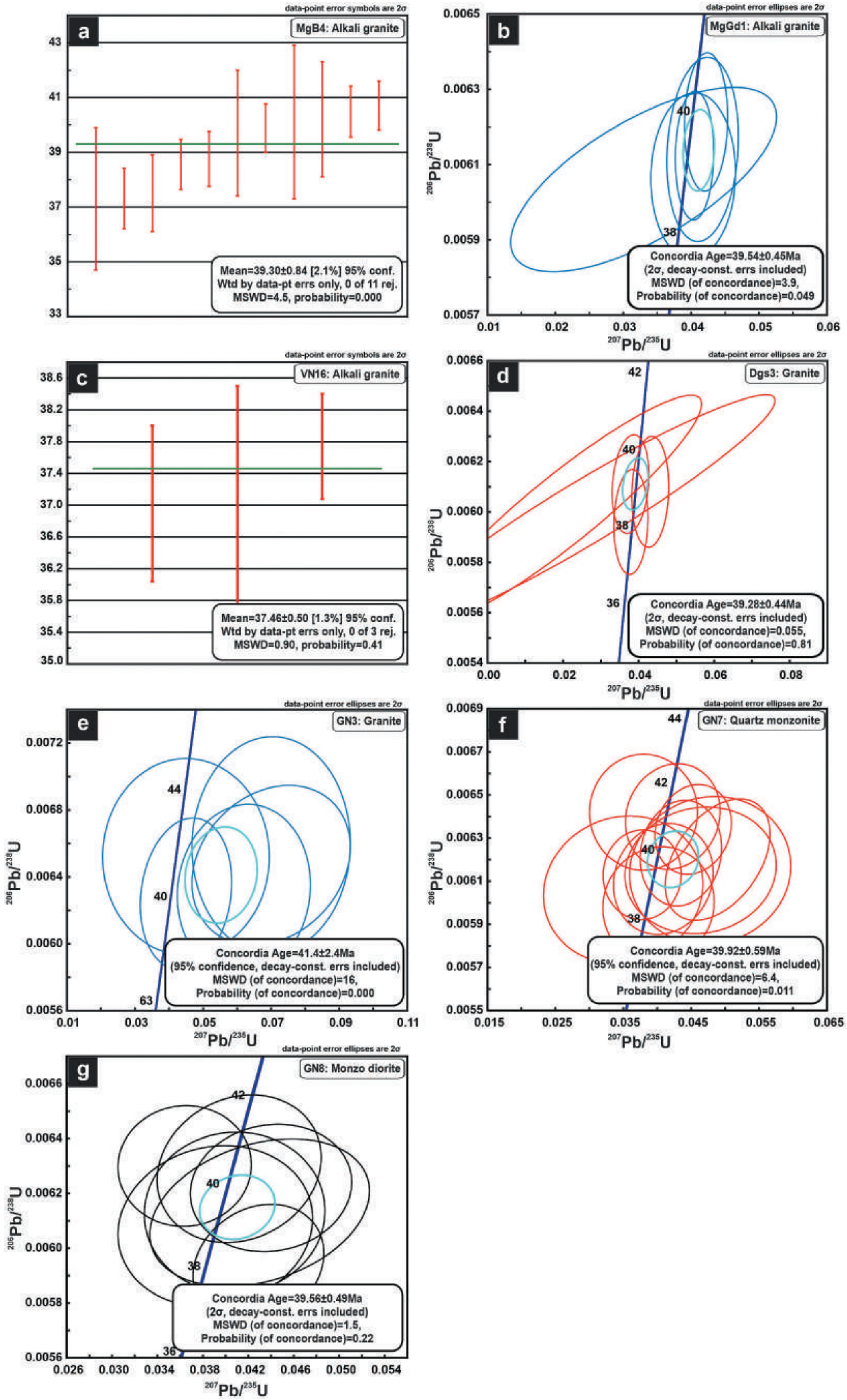

Figure 6. Concordia diagrams and weight mean diagrams (a, c) for plutonic samples of the studied region (samples (a) MgB4 (alkali feldspar granite), (b) MgGd1 (alkali feldspar granite), (c) VN16 (alkali feldspar granite), (d) Dgs3 (granite), (e) GN3 (granite), (f) GN7 (quartz monzonite), and (g) GN8 (monzodiorite)).

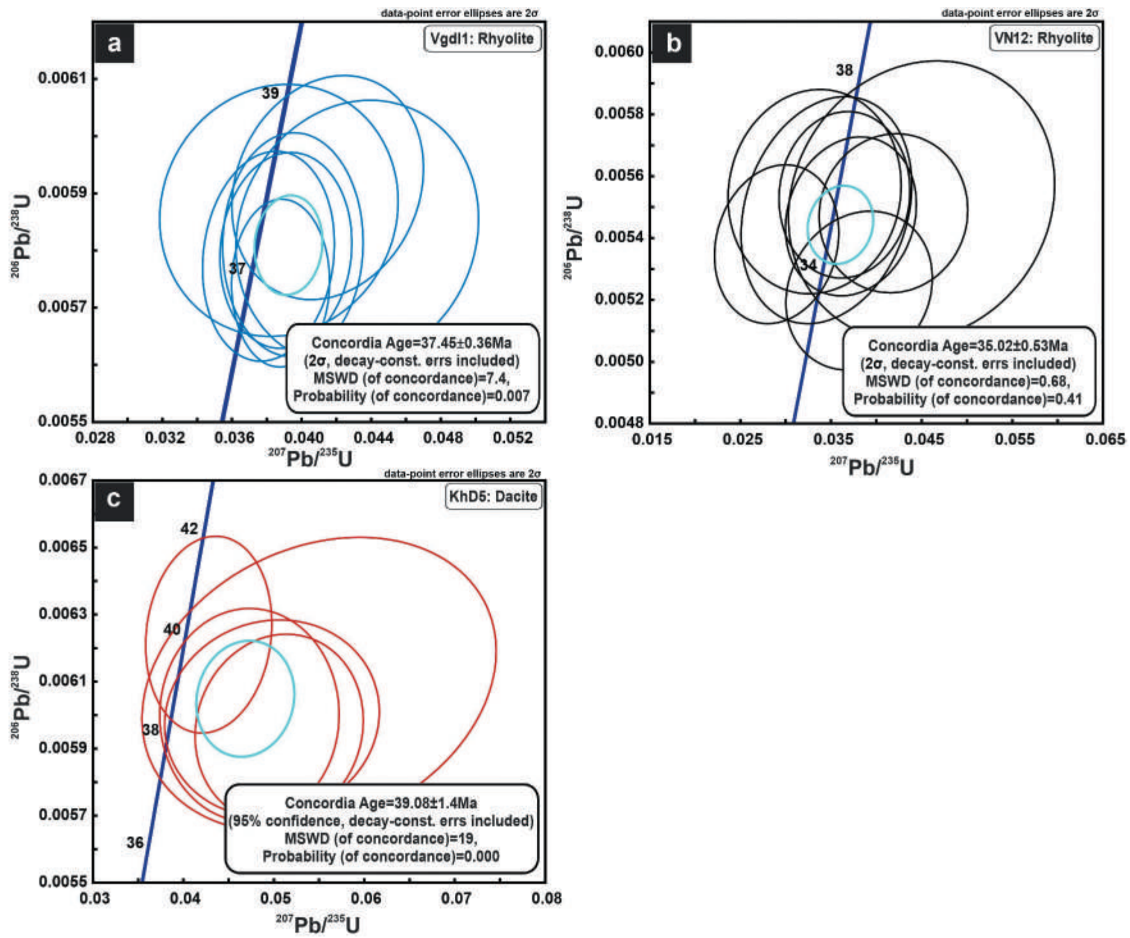

Figure 7. Concordia diagrams for volcanic samples of the studied region (samples (a) Vgd1, rhyolitic sample, (b) VN12, rhyolitic sample and (c) KhD5, dacitic sample).

rocks of Cenozoic age exist (Mazhari *et al*. 2009; Mazhari *et al*. 2011; Azizi *et al*. 2011; Mahmoudi *et al*. 2011; Sepahi *et al*. 2014; Rezaei *et al*. 2021. Numerous dating of Palaeogene rocks has been performed in recent years in the mentioned regions, which are summarized below:

Geochronology of Paleogene magmatic rocks from UDMA

Magmatism in the UDMA was most active and widespread in the Eocene and Oligocene, ca. 55–25 Ma (during ~30 m.y.) (Chiu *et al*. 2013). According to U-Pb data on zircon obtained over the last decade, a majority of intrusive rocks in the UDMA yielded Tertiary ages (mostly ranging from early Eocene to late Miocene) (e.g. Chiu *et al*. 2013; Honarmand *et al*. 2014; Sarjoughian and Kananian 2017). This indicates relatively continuous plutonism at such a time possibly due to shifting subduction zone from neighbouring Sanandaj-Sirjan arc to UDMA.

New data confirm that the magmatism in the south-eastern parts of the UDMA can be divided into two distinct periods: i.e. during ~ 80–70 Ma (Late Cretaceous) and ~ 50–1.2 Ma (Eocene to Pleistocene), but with a magmatic flare-up in the Eocene (Shafaii Moghadam *et al*. 2022).

According to Sepidbar *et al*. (2019), the UDMA main front flared-up at ~ 54–37 Ma and 20–5 Ma, overlapping its rare-arc magmatic flare-ups at 45–40 Ma and 30–25 Ma.

In the northern half of UDMA, about 60 km north-west of Saveh (sample 3 in Figure 1), Verdel *et al*. (2011) obtained a U- Pb age of 54.7 ± 3.1 Ma for zircons from an andesite flow near the base of the volcanic section, which is the best estimate for the age of the oldest arc volcanism in the Palaeogene. Slightly higher in sequence, they obtained an age of 50.9 ± 4.4 Ma for green tuff. Ages decrease up section and reach 44.3 ± 2.2 Ma in the middle of the volcanic section and 37.3 ± 1.2 Ma in the upper part of the volcanic sequence.

At the northern part of the UDMA (sample 4 in Figure 1), U-Pb zircon data by Ahmadi *et al*. (2021) show 46.6 ± 4.6 to 47.1 ± 4.5 Ma for diorite sample and 37.1 ± 1.2 to 38.57 ± 0.41 Ma for the granodiorite sample. In this area, for the Shahjahan batholith, Jamshidibadr and Hassanpour (2015) reported 40.52 ± 0.44 and 46.4 ± 2.6 Ma intrusive ages for granodiorite and granite plutons, respectively, based on Ar-Ar age dating on biotite.

In the southeast UDMA, in Nain area (sample 5 in Figure 1) volcanic samples were dated by Chiu *et al*. (2013) and yielded U–Pb zircon ages of 37.0 ± 0.4 Ma in the Late Eocene. Beside the Batlaqe-Gavkhuni, three andesites sampled from different volcanic domes yielded identical Late Eocene ages of ~35 Ma and a black tuff gave a similar age of 37.8 ± 0.6 Ma (Chiu *et al*. 2013) (sample 6 in Figure 1). A Middle Eocene age of 42.9 ± 0.4 Ma was obtained by an andesite from ~80 km southeast of Nain (sample 7 in Figure 1). A Late Eocene age of 37.6 ± 0.5 Ma was obtained for an andesitic lava, ~50 km north of the Sirjan (sample 8 in Figure 1). In the SE segment of the UDMA near Nagisun, south of Bam (sample 9 in Figure 1), U-Pb zircon ages show comparable ages for both plutonic (~34–25 Ma) and volcanic (~34–27 Ma) rocks (Shafaii Moghadam *et al*. 2022). U-Pb zircon dating of Sarduiyeh granitoid in SE of the UDMA (sample 10 in Figure 1) yield an age of 27.95 ± 0.27 Ma (Nazarinia *et al*. 2018.

Geochronology of SSZ Paleogene magmatic rocks

Chiu *et al*. (2013) consider that Palaeogene ages from ca. 60 to 35 Ma are available in the northwestern part of the SSZ. In contrast in the southeastern SSZ, Cenozoic igneous rocks do not exist. This seems to support the idea of dividing the SSZ into two parts (Eftekharnejad 1981; Ghasemi and Talbot 2006): (1) the South SSZ that consists essentially of rocks deformed and/or metamorphosed in the Triassic and Jurassic; and (2) the North SSZ that was deformed in the Late Cretaceous and intruded by Cenozoic felsic rocks in some localities. Hassanzadeh and Wernicke (2016) believe that the Cretaceous-Palaeogene magmatism occurred in the northwestern SSZ and it appears to be a continuation of the Jurassic event.

In the northern SSZ, in addition to Jurassic plutonic bodies, there are some Eocene granitoid bodies such as Naghadeh granitoid (sample 11 in Figure 1) with 41.85 ± 0.81 Ma zircon U-Pb age (Mazhari *et al*. 2011), intrusive rocks of ~41 Ma from the Piranshahr (sample 12 in Figure 1) (Mazhari *et al*. 2009), Marivan granitoid (sample 13 in Figure 1) with ~38 Ma zircon U-Pb age (Sepahi *et al*. 2014; Rezaei *et al*. 2021, granitoids of ~ 37–35 Ma from Taa–Baysaran of Kamyaran (sample 14 in Figure 1) (Azizi *et al*. 2011), Baneh granites (sample 15 in Figure 1) with zircon U-Pb ages of 39.7 ± 0.9 Ma, 40.5 ± 0.6 Ma, and 41.0 ± 1.0 Ma (Azizi *et al*. 2018) and a quartz monzodiorite at 34.9 ± 0.1 Ma from the Gosheh–Tavandasht complex (sample 16 in Figure 1) (Mahmoudi *et al*. 2011).

Azizi *et al*. (2018) suggest that igneous rocks of the Baneh complex were injected in a transpressional tectonic regime along the Zagros Fault in northwest Iran and the compositional similarity of these granites to global syn-collision granites confirms the association of them with collision of the Arabian and Eurasian plates in northwest Iran.

Geochronology of AMA Paleogene magmatic rocks

The oldest age reported byAxen *et al*. (2001) from the shoshonitic plutonic association of the AMA is a 56 ± 2 Ma U-Pb zircon age for Akapol quartz monzonitic intrusion in the central part of AMA (sample 17 in Figure 1).

Ballato *et al*. (2011) showed that at the base of Karaj Formation, in the central part of AMA (sample 18 in Figure 1), zircons in andesites yield an age of 47.4 ± 3.8 Ma and biotite from a fine-grained green tuff at the top of this formation has an age of 36.0 ± 0.2 Ma. Verdel *et al*. (2011) obtained similar geochronological data in a similar area along the Chalus road transect (sample 19 in Figure 1). In this region, zircons yield U-Pb ages of 49.3 ± 2.9 Ma in the middle tuff member, 45.3 ± 2.3 Ma in the Asara shale, and 41.1 ± 1.6 Ma in the upper tuff member. Also, they reported ages of 39.3 ± 0.2 Ma and 36.8 ± 0.1 Ma $^{40}Ar/^{39}Ar$ magmatic cooling ages for biotite and alkali feldspar from monzonitic sill, respectively, in this area and $^{40}Ar/^{39}Ar$ ages of 38.47 ± 0.10 for the Lavasan intrusive body in NE Tehran (sample 20 in Figure 1).

Vincent *et al*. (2005) have published similar Ar-Ar ages of 41–38 Ma for four basalts and an andesite within the volcanic succession from the Talesh in the Azerbaijan region (sample 2 in Figure 1).

In Sabalan-Astara areas (sample 21 in Figure 1), Chiu *et al*. (2013) obtained 42.1 ± 0.3 and 44.5 ± 0.2 Ma ages, by dating two basaltic samples using Ar-Ar method. A basaltic andesite from the southwest of Qazvin (sample 22 in Figure 1) yielded zircon U-Pb age of 35.8 ± 0.3 Ma in the Late Eocene.

From the west AMA, SE Ahar (sample 23 in Figure 1), the subalkali basalts and andesites are dated to 57.0 ± 1.2 Ma, and are likely derived from a supra-subduction mantle wedge. Later, trachytic A-type rocks erupted from ~42 to 25 Ma during an anorogenic (extensional) stage triggered by slab retreat and associated asthenospheric mantle influx (Ahmadvand *et al*. 2020). This extension led to localized upwelling of the asthenosphere, providing the heat required for partial melting of the subduction-contaminated subcontinental lithospheric mantle beneath the Alborz magmatic belt.

The dating performed by Nabatian *et al*. (2014) in the west of AMA shows the age of 41.1 ± 1.9 Ma for the Zaker quartz monzonite (sample 24 in Figure 1) and the ages of 42.56 ± 0.62 and 39.0 ± 1.1 Ma for the Zanjan quartz monzodiorite (sample 25 in Figure 1). In the central part of AMA, Davari (1987) reported K-Ar age of 41 ± 4 Ma for Ghasrefirozeh granitoid (sample 26 in Figure 1).

By studying and dating several plutons of the Tarom-Arasbaran batholiths (west of AMA), Castro *et al*. (2013) concluded that the Taroum plutonism is about 10–15 Ma older than Arasbaran monzonitic plutonism. They think that individual plutons were emplaced over a short time period of ca. 15 Ma (from 38 to 23 Ma) along Late Eocene-Oligocene times (with an age progression from SE to NW at a rate of 2 cm/year). According their study, the age of Tarom-Arasbaran batholiths decreases from east (Abhar ca. 38 Ma) to west (Shaivar-Dagh ca. 23 Ma).

In the western parts of the AMA (Arasbaran), Aghazadeh *et al*. (2011) reported a LA-ICP-MS Concordia zircon age of 30.8 ± 2.1 Ma for the calc-alkaline granodioritic rocks and a range from 23.3 ± 0.5 to 25.1 ± 0.9 Ma for the shoshonitic association (sample 27 in Figure 1).

The Siah-Kamar Mo deposit at the northwestern AMA (Mianeh) (sample 28 in Figure 1) is characterized by the emplacement of a multiphase Oligocene basic/intermediate (at ca. 33–30 Ma) to acidic (29–28 Ma) magmatic suite, which intruded the Eocene volcanic country rocks (Rabiee *et al*. 2019).

Based on our U-Pb zircon dating, all rocks of the study area (Takestan, location 1 in Figure 1) as part of western Alborz were generated in the Late Eocene. Most granitoid bodies and dacitic sample were emplaced and crystallized during the Bartonian (38–41.3 Ma). A small part of these granitoid bodies with alkaline granite composition (VN16 sample) and rhyolitic samples were produced at Periabonian (33.9–38.0 Ma). These data indicate that dacitic and plutonic rocks are contemporaneous and, therefore, are co-magmatic whereas the rhyolitic rocks and a small part of the granitoid rocks are slightly younger than the other plutonic and dacitic rocks. The presence of ignimbrites, as well as dacitic and rhyolitic domes, is evidence of the occurrence of caldera in this area. Accordingly, after the formation of plutonic rocks, magma ascends through fractures and faults as rhyolitic domes and ignimbrite flows due to caldera collapse.

The age range of the Palaeogene magmatic rock samples in Iran is from 56 to 23 Ma. The ages obtained for the samples of the studied area range from 41 to 37 Ma and are in the Late Eocene, which are within the age range of the other samples of Palaeogene of Iran.

According to previous studies (such as Asiabanha and Foden 2012; Castro *et al*. 2013), after the Late Palaeogene, several intrusive bodies have been injected into the Palaeogene volcanic rocks in the AMA, which are usually small in volume (as dyke, stock, and laccolith). According to Aghanabati (2004), it is possible that most of the granitic magmas to be result of the fractional crystallization of the Eocene basalts. This means that most of the granitic magmas are situated in the roots of Eocene lavas. In addition, some of the granitic magmas may have originated from crustal melting.

Magmatic activity appears to have been greatest in the western Alborz, and diminished towards the east (Rezaeian 2008). As mentioned before, the oldest Palaeogene plutonic rock in the Alborz is the Akapol quartz monzonitic intrusion (sample 17 in Figure 1) in the central part of AMA with a 56 ± 2 Ma U – Pb zircon age (Axen *et al*. 2001). The Ghasrefirozeh granitoid (sample 26 in Figure 1) in the central part of AMA has K-Ar age of 41 ± 4 Ma (Davari 1987). In the West of AMA, the Zaker quartz monzonite (sample 24 in Figure 1) has age of 41.1 ± 1.9 Ma and Zanjan quartz monzodiorite (sample 25 in Figure 1) has ages of 42.56 ± 0.62 and 39.0 ± 1.1 Ma (Nabatian *et al*. 2014). The $^{40}Ar/^{39}Ar$ ages of the Lavasan intrusive body in NE Tehran (sample 20 in Figure 1) by Ballato *et al*. (2011) indicate magmatic emplacement at 38.47 ± 0.10 Ma.

Castro *et al*. (2013) have postulated that in western Alborz magmatic rocks of Palaeogene age became older from west to east. Considering that the granitoid rocks of Takestan area (west of the AMA) with zircon U-Pb ages of 41–39 Ma are located in the east of Abhar granitoid with zircon U-Pb ages of ca.38 Ma (Castro *et al*. 2013), it seems that the idea of Castro *et al*. (2013) about increasing of the age of the plutonic rocks of the western AMA to the east is correct (i.e. Akapol quartz-monzonite with a 56 ± 2 Ma age is situated in the east and Shaivar-Dagh granitoid with a 23 Ma age is in the west).

Geochronology of Lut block and eastern Iran paleogene magmatic rocks

For the Koudakan granitoid in the Lut block (sample 29 in Figure 1), the U-Pb zircon geochronology of monzodiorite and tonalite rocks reveals the crystallization ages of 41.7 ± 3.4 to 37.88 ± 0.77 Ma (Bartonian) (Omidianfar *et al*. 2018). According to Omidianfar *et al*. (2018) the Koudakan intrusion like other Eocene to Oligocene granitoids in the Lut block formed in a post-collisional tectonic environment after a subduction event. Abundant Eocene and Oligocene volcanism in the Lut block of eastern Iran may have developed in a similar tectonic setting as suggested by Jung *et al*. (1984).

LA MC-ICP-MS U-Pb zircon data from a diorite in the Mahoor granitoid rocks (Lut Block, sample 30 in Figure 1) yielded similar Concordia ages of ca. 31.88 ± 0.20 Ma, which corresponds to the Oligocene period (Beydokhti *et al*. 2015). Geochronology using the U-Pb zircon method on a pyroxene diorite porphyry stock and two granite porphyry dikes in the Simorgh prospecting area, Lut Block (sample 31in Figure 1), revealed 24.85 ± 0.51 Ma, 25.37 ± 0.56 Ma, and 25.94 ± 0.76 Ma ages, respectively (late Oligocene, Chattian) (Borabadi *et al*. 2018). According to U-Pb age dating by Shahbazi *et al*. (2021), the Aliabad Daman granitoid pluton at the southern edge of the Sabzevar zone in the northeast of Iran (sample 32 in Figure 1), has given 45–40 Ma ages (i.e. middle Eocene; Lutetian to Bartonian). In the other parts of Sabzevar zone, Eocene granitoids (ca. 40 Ma) were reported, too (sample 33 in Figure 1) (Shafaii Moghadam *et al*. 2015; Almasi *et al*. 2019. Laser ablation spots from the three analysed dacitic samples in Sabzevar (sample 34 in Figure 1) yielded ages of ca. 43.5–47 Ma, corresponding to the Middle Eocene (Shafaii Moghadam *et al*. 2016). Kashmar calc-alkaline granitoids in the south of the Sabzevar suture zone (sample 35 in Figure 1) have ages of ca. 40–41 Ma (Shafaii Moghadam *et al*. 2015).

Probable temporal geodynamic evolution of the region

The temporal distribution of Cenozoic (mainly Eocene to Quaternary) magmatic rocks in the Alborz occurs as several magmatic pulses in the Eocene, Miocene, and Plio-Quaternary (Asiabanha and Foden 2012). The products of extensive Eocene volcanic eruptions in the western and central parts of Alborz were primarily described by Dedual (1967) as the 'Karaj Formation' (e.g. Berberian 1983; Hassanzadeh *et al*. 2002; Allen *et al*. 2003; Ballato *et al*. 2011). Development of the Eocene normal faults in the Alborz Mountains (Guest *et al*. 2006), and stratigraphic evidence of Eocene subsidence in the Alborz Mountains and central Iran block, has been attributed to Eocene extension (Brunet *et al*. 2003; Hassanzadeh *et al*. 2004; Vincent *et al*. 2005; Guest *et al*. 2007; Morley *et al*. 2009). The Eocene volcanic pile in the AMA (Karaj Formation) was formed as shallow subaqueous volcaniclastic deposits (mostly in central Alborz) followed by sub-aerial lava flows (mostly in the western Alborz) (Asiabanha 2006). The stratigraphy of the southern Alborz indicates that this area returned to marine conditions in the Paleocene, which continued throughout the Eocene. These deposits have significant volcaniclastic components akin to the sources located within northern Iran (Rezaeian *et al*. 2012). In the Middle Eocene, despite the dominance of pyroclastic sediments in Alborz, lava flows and intrusive bodies have been also formed. For example, Tarom, Lavasan, and Qasr-e-Firuzeh intrusions, with the emplacement ages of 35–40 Ma were formed in this time (Davari 1987; Rezaeian 2008; Ballato *et al*. 2011). The thickness of lava flows and the ratio of lava flow to pyroclastic rocks increase to the west (Asiabanha and Foden 2012). The above interpretation is consistent with the occurrence of thick Paleocene-Eocene turbidites (>5 km) (Allen *et al*. 2003), which decrease to a thickness of 3 km in the east (Brunet *et al*. 2003). The composition of these lava flows is basic to acidic and includes trachybasalt, trachyandesite, dacite, and rhyolite. Red soil horizons under the mafic lava flows, together with columnar jointing are common in this part of Alborz, suggesting that they are the products of sub-aerial eruptions (Asiabanha and Foden 2012).

During the Late Eocene-Early Oligocene (□34 Ma), submarine volcanoclastic sedimentation stopped in the Alborz. This transition from extension to compression in Iran and adjacent areas, accompanied by the regional termination of the voluminous arc and back-arc magmatism (Ballato *et al*. 2011), is attributed to the beginning of the Arabia-Eurasia intercontinental collision (Hessami *et al*. 2001; Brunet *et al*. 2003; Vincent *et al*. 2007; Morley *et al*. 2009). The presence of evaporative gypsum lenses on the top of the pyroclastic sediments of Karaj Formation throughout Alborz (such as Gachsar and Alamut areas) accompanied by strong folding of tuffs in Alamut (Qazvin) and Jirandeh (Lushan) shows that the sedimentary-volcanic basin of the Late Eocene has been uplifted and eroded during compressive tectonics (Asiabanha and Foden 2012). Rezaeian *et al*. (2012), by calculating the exhumation rates of Alborz in the Palaeogene and Neogene times, showed that this exhumation rate was lower in the Early Oligocene to the Early Miocene, but was higher in the Eocene and Middle Miocene. A transition from extension to compression in the region possibly occurred at the Eocene-Oligocene boundary (Vincent *et al*. 2005, 2007; Ballato *et al*. 2008). The nearly synchronous onset of (1) rapid south Caspian subsidence (Nadirov *et al*. 1997), (2) cooling, exhumation, and uplift of the west-central Alborz (Axen *et al*. 2001), and (3) coarse molasse deposition in the Zagros foreland basin (Dewey *et al*. 1973; Beydoun *et al*. 1992) all record the widespread onset of rapid vertical motions in latest Miocene time. Axen *et al*. (2001) inferred that uplift of the high Alborz and Talesh Mountains loaded the south Caspian basin, causing accumulation of thick Late Cenozoic deposits.

According to some researchers (such as Berberian and Berberian 1981; Aghazadeh et al. 2010, 2011; Asiabanha and Foden 2012) in the northwestern and central parts of the AMA, Oligo-Miocene plutonic rocks are typically post-collisional that are formed after the main orogenic events.

In contrast to a typical Andean-type convergent margin, the Iranian Palaeogene arc experienced strong extension throughout its evolution (Sepidbar *et al*. 2019). An extensional period may have been resulted from Palaeogene slab roll-back (Shafaii Moghadam and Stern 2011; Shafaii Moghadam *et al*. 2018. The slab roll-back can be associated with extension, crustal thinning, and juvenile crustal addition (Miskovic and Schaltegger 2009). The slab break-off may also be other reason for extension in the region (Deevsalar *et al*. 2017). The change in the slab dip of the subducting Neotethyan lithosphere from Late Cretaceous to present can also be another alternative model, which can explain the spatial distribution of Palaeogene magmatic rocks of Iran (Verdel *et al*. 2007; Sepidbar *et al*. 2019).

Verdel *et al*. (2011) suggested that Palaeogene magmatism in Iran was driven by an episode of slab break-off or slab rollback. These events could have caused mantle upwelling and may have significantly changed the thermal structure of the mantle wedge, and abundant Palaeogene magmatic rocks originating from different magmatic sources were generated during these events.

Subduction and Andean-type arc magmatism began in late Triassic/Early Jurassic time, culminating at ~170 Ma. The extinction of arc magmatism in the SSZ, and its shift northeastward to form the subparallel UDMA, occurred diachronously along strike, in Late Cretaceous or Palaeogene time (Hassanzadeh and Wernicke 2016). According to Rabiee *et al*. (2020), the magmatic assemblages in the NW of Iran are located along the transverse tectonic structures of the fault systems, which segment the continental lithosphere of the Iranian plateau. Inherited plate boundaries and pre-existing regional faults provide efficient zones for facilitating magma ascent (Richards 2003; Rabiee *et al*. 2020).

After intense plutonism in Jurassic (Mesozoic arc) in the SSZ, there is a period of magmatic gap or minimal magmatic activities until Palaeogene in the region. Flat subduction or slab break off may have been cause of this gap during Cretaceous. It is worthy to note that some authors (e.g. Azizi and Stern 2019) did not believe in cessation of Jurassic magmatism due to subduction and prefer rifting model for the interpretation of magmatism in this period. Also, Lucci *et al*. (2023) introduced a continental rifting model coupled with mantle plume activity for interpretation of mafic plutonism in central SSZ.

We accept the opinion of a subduction with roll back model by Verdel *et al*. (2011) about Palaeogene magmatism of Iran, because there is contemporaneous magmatism in a widespread part of Iran including Sanandaj-Sirjan, Urumieh-Dokhtar and Alborz tectono-stratigraphic zones in such a time especially in Eocene (Fig. 9). For examples, Sepahi *et al*. (2014) reported a pluton with Eocene age (~38 Ma zircon U-Pb age) in Marivan region in the SSZ. In the northern part of the UDMA, U-Pb zircon data by Ahmadi *et al*. (2021) reported 46.6 ± 4.6 to 47.1 ± 4.5 Ma for diorite sample and 37.1 ± 1.2 to 38.57 ± 0.41 Ma for the granodiorite sample. In the same area, for the Shahjahan batholith, Jamshidibadr and Hassanpour (2015) reported 40.52 ± 0.44 and 46.4 ± 2.6 Ma for granodiorite and granite plutons. In the southeast UDMA, in Nain area volcanic samples, which were dated by Chiu *et al*. (2013), have U-Pb zircon ages of 37.0 ± 0.4 Ma. Also, our studied samples indicate plutonic rocks in the same time interval (39–41 Ma) in the AMA. Therefore, a simple subduction model with roll back of subducting slab which is presented in Figure 8 (modified and redrawn according to Verdel *et al*. (2011)), may explain the observed nearly simultaneous age ranges for major Palaeogene magmatic rocks.

According toVerdel *et al*. (2011), during the Palaeogene (66–23 Ma), synvolcanic subsidence occurred in Iran, which is indicated by the presence of shallow marine sediments interbedded with Palaeogene volcanic accumulations (Stöcklin 1968; Berberian and King 1981; Emami 1991) and submarine volcanism (e.g. Förster *et al*. 1972; Amidi *et al*. 1984; Spies *et al*. 1984; Hassanzadeh 1993). Rapid subsidence at this time is attributed to the slab rollback of the subducting Neotethys oceanic lithosphere (Vincent *et al*. 2005; Verdel *et al*. 2011. Roll-back of the oceanic slab and the accompanying extension occur when the subduction velocity is greater than the convergence velocity (Schellart 2005). According to Emami (2000), volcanism was at its most intense period in the Middle Eocene. This phase of magmatism is characterized by magmatic rocks with intermediate compositions showing calc-alkaline to potassic affinity, which occur in an arc/back-arc system or extensional arc environment (Berberian 1983; Kazmin *et al*. 1986; Allen *et al*. 2003; McQuarrie *et al*. 2003; Hassanzadeh *et al*. 2004; Vincent *et al*. 2005; Verdel *et al*. 2011; Allen *et al*. 2013).

Chiu *et al*. (2013) suggested that volcanism in the UDMA, Alborz Range, Central Iran and Lut block were most active and widespread during the Eocene and Oligocene (ca. 55–25 Ma). This volcanism would require a protracted, and steady, subduction system that started since the Early Eocene. In the northern Sistan and Lut regions the presence of widespread calc-

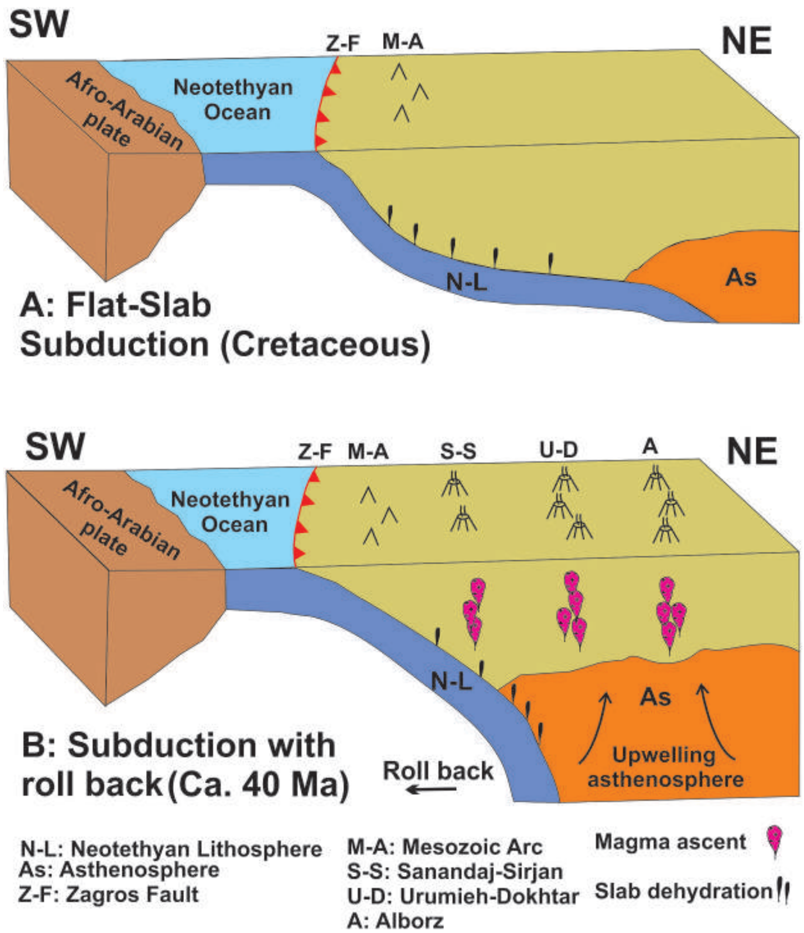

Figure 8. Simple cartoons showing possible tectono-magmatic environment of the region, (a): in the Cretaceous, (b): in the Paleogene (modified and redrawn after Verdel *et al.* 2011).

alkaline volcanism during ca. 45–25 Ma may be resulted from an extensional tectonic environment post-dating the suturing between the Lut and Afghan blocks (Zarrinkoub et al. 2010, 2012; Pang et al. 2011, 2012). Shafaii Moghadam *et al.* (2023) suggest that slab roll-back along with upper-plate extension, partial melting of the subducting slab, and a high temperature asthenospheric mantle flowing into the wedge during the Early to Middle Eocene controlled the generation and eruption of the high-K magmas in NE Iran, in a back-arc setting behind the Urumieh-Dokhtar magmatic belt.

A transition from weak extension to compression in tectono-stratigraphic units of northern part of Iran occurred around ~36 Ma (Vincent *et al.* 2005; Vincent *et al.* 2007; Guest *et al.* 2007; Ballato *et al.* 2008) however, the deformation related to this event was not strong enough to exhume deeper crustal rocks, but resulted in reactivation and inversion of normal faults under the new compressional regime (Morley *et al.* 2009). The bending of the Talesh Mountains in west Alborz was earlier than eastern Alborz, Kopeh Dagh, and central Alborz Mountains that was initiated during the late Cenozoic (Madanipour *et al.* 2017).

Based on the above studies, it can be concluded that this bending has caused Alborz to deviate from the direct trend to create the bending of the Takestan region (location 1 in Figure 1) and the S-shaped bend of the Talesh mountains (location 2 in Figure 1). Because of this bending, the direct trend of injected intrusive bodies from the Central Alborz to the Western Alborz has probably been changed and the present day curvature has been created.

Conclusion

Magmatic rocks of the Takestan area are a suite of co-magmatic plutonic and volcanic rocks. Zircon U-Pb LA ICP-MS dating shows that most Takestan plutonic rocks were emplaced at 39–41 Ma (Late Eocene, Bartonian). A small part of these rocks has an age of ~37 Ma (Late Eocene, Priabonian). The dacitic rocks have age of ~39 Ma (Late Eocene, Bartonian) and the rhyolites are the youngest part of the magmatic rocks of the region with ages of 37–35 Ma (Late Eocene, Priabonian). Older zircons, as early crystallized components of a long-lived magma chamber and/or inherited zircons from older continental crust, are also present in many samples except KhD5 sample (dacite). The ages of the samples of the studied area range from 41 to 37 Ma and are in the Late Eocene, which resemble the age range of the other samples of Palaeogene of Iran. The studied rocks, like other Palaeogene magmatic rocks in Iran, were possibly formed as a result of a subduction tectonic environment (with occasional roll back of the subducting slab), related to the evolution of Neotethyan lithosphere.

Acknowledgements

We are thankful of Prof. Lorence G. Collins for editing former version of the manuscript. Also, we appreciate good reviews and comments by Federico Lucci and an anonymous reviewer which elevated the scientific level of the paper. Hamed Vahidpour has contribution in drawing and raising quality of Figures and formatting the primary version of the manuscript and therefore we kindly appreciate him.

Disclosure statement

No potential conflict of interest was reported by the author(s).

Funding

This work has been supported by grants awarded to Ali A. Sepahi by Bu-Ali Sina University in 2020 and by instrumental help of the University of New Brunswick in agreement by Chris McFarlane.

ORCID

Ali A. Sepahi http://orcid.org/0000-0002-3075-8416

Author contributions

A.A.S: Project administration; A.A.S: Conceptualization and Visualization; A.A.S, A.A, and B.N: Field work and petrography; A.A.S, C.R.M: Methodology and Geochronology; A.A.S, A.A and B.N: Investigations and Data curation; A.A.S Formal analysis; A.A.S, B.N and D.L: writing original manuscript, review and editing.

Data availability statement

Data generated or analysed during this study are provided in full within the published article.

References

Agard, P., Monie, P., Gerber, W., Omrani, J., Molinaro, M., Labrousse, L., Vrielynck, B., Meyer, B., Jolivet, L., and Yamato, P., 2006, Transient synobduction exhumation of Zagros blueschists inferred from pressure, temperature, deformation, time and kinematic constraints: Implications for Neotethys wedge dynamics: Journal of Geophysical Research, v. 111, p. B11401. 10.1029/2005JB004103.

Agard, P., Omrani, J., Jolivet, L., Whitechurch, H., Vrielynck, B., Spakman, W., Monie, P., Meyer, B., and Wortel, R., 2011, Zagros orogeny: A subduction-dominate process: Geological Magazine, v. 148, no. 5–6, p. 692–725. 10.1017/S001675681100046X.

Aghanabati, S.A., 2004, Geology of Iran: Tehran, Geological Survey of Iran (in Persian).

Aghazadeh, M., Castro, A., Badrzadeh, Z., and Vogt, K., 2011, Post-collisional polycyclic plutonism from the Zagros hinterland: The Shaivar Dagh plutonic complex, Alborz belt, Iran: Geological Magazine, v. 148, no. 5–6, p. 980–1008. 10.1017/S0016756811000380.

Aghazadeh, M., Castro, A., Omran, N.R., Emami, M.H., Moinvaziri, H., and Badrzadeh, Z., 2010, The gabbro (shoshonitic)-monzonite-granodiorite association of Khankandi pluton, Alborz Mountains, NW Iran: Journal of Asian Earth Sciences, v. 38, no. 5, p. 199–219. 10.1016/j.jseaes.2010.01.002.

Aguirre-Díaz, G.J., Labarthe-Herna´ndez, G., Trista´n-Gonza´lez, M., Nieto-Obrego´n, J., and Gutie´rrez-Palomares, I., 2008, The Ignimbrite Flare-Up and Graben Calderas of the Sierra Madre Occidental, Mexico, Elsevier: Developments in Volcanology, v. 10, p. 143–178.

Ahmadi, Z., Jahangiri, A., Moazzen, M., and Whan Oh, C., 2021, Eocene arc-related magmatism within the Neotethys subduction System in NW Iran: Geochemistry and SHRIMP zircon U-Pb Dating on Magmatic Phases in the Shahjahan Batholith. P., 1–25 p. 10.21203/rs.3.rs-712384/v1.

Ahmadvand, A., Ghorbani, M.R., Mokhtari, M.A.A., Chen, Y., Amidon, W., Santos, J.F., and Paydari, M., 2020, Lithospheric mantle, asthenosphere, slab and crustal contribution to petrogenesis of Eocene to Miocene volcanic rocks from the west Alborz magmatic assemblage, SE ahar, Iran: Geological Magazine, v. 158, no. 3, p. 1–32. 10.1017/S0016756820000527.

Alai Mahabadi, S., and Fanoudi, M., 1992, Geology of the Takestan quadrangle: Geological Survey of Iran. scale 1: 100000, 1 sheet.

Allen, M., 2010, Roles of strike-slip faults during continental deformation: Examples from the active Arabia-Eurasia collision: Journal of the Geological Society of London, Special Publication, v. 338, p. 329–344. 10.1144/SP338.15.

Allen, M.B., and Armstrong, H.A., 2008, Arabia – Eurasia collision and the forcing of mid-Cenozoic global cooling: Palaeogeogr Palaeoclim Palaeoecol, v. 265, no. 1–2, p. 52–58. 10.1016/j.palaeo.2008.04.021.

Allen, M.B., Ghassemi, M.R., Shahrabi, M., and Qorashi, M., 2003, Accommodation of late Cenozoic oblique shortening in the Alborz range, northern Iran: Journal of Structural Geology, v. 25, no. 5, p. 659–672. 10.1016/S0191-8141(02)00064-0.

Allen, M.B., Kheirkhah, M., Neill, I., Emami, M.H., and McLeod, C. L., 2013, Generation of arc and within-plate chemical signatures in collision zone magmatism: Quaternary lavas from

Kurdistan Province, Iran: Journal of Petrology, v. 54, no. 5, p. 887–911. 10.1093/petrology/egs090.

Almasi, A., Karimpour, M.H., Arjmandzadeh, R., Khosrow, E., and EBRAHIMI NASRABADI, K., 2019, Zircon U-Pb geochronology, geochemistry, sr-nd isotopic compositions and tectonomagmatic implications of nay (NE Iran) post-collisional intrusives in Sabzevar zone: Turkish Journal of Earth Sciences, v. 28, no. 3, p. 372–397. 10.3906/yer-1805-36.

Amidi, S.M., Emami, M.H., and Michel, R., 1984, Alkali character of Eocene volcanism in the middle part of central Iran and its geodynamic situation: Geologische Rundschau, v. 73, p. 917–932. 10.1007/BF01820882.

Annells, R.N., Arthurton, R.S., Bazely, R.A., and Davis, R.G., 1975, Explanatory text of the Qazvin and Rasht quadrangles map: Geological Survey of Iran, Scale, v. 1. 250000, 1 sheet.

Arvin, M., Pan, Y., Dargahi, S., Malekizadeh, A., and Babaei, A., 2007, Petrochemistry of the Siah-Kuh granitoid stock southwest of Kerman, Iran: Implications for initiation of Neotethys subduction: Journal of Asian Earth Sciences, v. 27, p. 1–9. 10.1016/j.jseaes.2007.01.001.

Arvin, M., and Robinson, P.T., 1994, The petrogenesis and tectonic setting of lava from baft ophiolitic melange, SW Kerman, Iran: Canadian Journal of Earth Sciences, v. 31, p. 824–834. 10.1139/e94-076.

Asiabanha, A., 2006, A Paleogene two-stage volcanism in the Alborz zone, Iran, Proceedings of International Conference on Continental Volcanism. Guangzhou, China.

Asiabanha, A., and Foden, J., 2012, Post-collisional transition from an extensional volcano-sedimentary basin to a continental arc in the Alborz ranges, N-Iran: Lithos, v. 148, p. 98–111. 10.1016/j.lithos.2012.05.014.

Asiabanha, A., Ghasemi, H., and Meshkin, M., 2009, Paleogene continental-arc type volcanism in north Qazvin, north Iran: Facies analysis and geochemistry: Neues Jahrbuch für Mineralogie - Abhandlungen, v. 186, no. 2, p. 201–214. 10.1127/0077-7757/2009/0144.

Axen, G.J., Lam, P.S., Grove, M., Stockli, D.F., and Hassanzadeh, J., 2001, Exhumation of the west-central Alborz Mountains, Iran, Caspian subsidence, and collision-related tectonics: Geology, v. 29, no. 6, p. 559–562. 10.1130/00917613(2001)029<0559: EOTWCA>2.0.CO;2.

Azizi, H., Haddad, S., Stern, R.J., and Asahara, Y., 2018, Age, geochemistry, and emplacement of the ~40-Ma Baneh granite–appinite complex in a transpressional tectonic regime, Zagros suture zone, northwest Iran: International Geology Review, v. 61, no. 2, p. 195–223. 10.1080/00206814.2017.1422394.

Azizi, H., and Stern, R.J., 2019, Jurassic igneous rocks of the central Sanandaj-Sirjan zone (Iran) mark a propagating continental rift, not a magmatic arc: Terra Nova, v. 31, p. 415–423. 10.1111/ter.12404.

Azizi, H., Tanaka, T., Asahara, Y., Chung, S.L., and Zarrinkoub, M.H., 2011, Discrimination of the age and tectonic setting for magmatic rocks along the Zagros thrust zone, northwest Iran, using the zircon U-Pb age and sr-nd isotopes: Journal of Geodynamics, v. 52, no. 3–4, p. 304–320. 10.1016/j.jog.2011.03.001.

Bagheri, S., and Stampfli, G.M., 2008, The anarak, Jandaq and Posht-e-Badam metamorphic complex in central Iran: New geological data, relationships and tectonic implications: Tectonophysics, v. 451, p. 123–155. 10.1016/j.tecto.2007.11.047tecto.2007.11.047.

Ballato, P., Nowaczyk, N.R., Landgraf, A., Strecker, M.R., Friedrich, A., and Tabatabaei, S.H., 2008, Tectonic control on sedimentary facies pattern and sediment accumulation rates in the Miocene foreland basin of the southern Alborz Mountains, northern Iran: Tectonics, v. 27, no. 6, p. 1–20. 10.1029/2008TC002278.

Ballato, P., Uba, C.E., Landgraf, A., Strecker, M.R., Sudo, M., Stockli, D.F., Friedrich, A., and Tabatabaei, S.H., 2011, Arabia-Eurasia continental collision: Insights from late tertiary foreland-basin evolution in the Alborz Mountains, northern Iran: Geological Society of America Bulletin, v. 123, no. 1–2, p. 106–131. 10.1130/B30091.1.

Barrier, E., Vrielynck, B., Brouillet, J., and Brunet, M., 2018, Paleotectonic reconstruction of the central tethyan realm. Tectonono-sedimentary-palinspastic maps from Late permian to Pliocene: CCGM/CGMW, Paris. CCGM/CGMW Paris (in France).

Belousova, E.A., Griffin, W.L., Suzanne, Y.O.R., and Fisher, N.I., 2002, Igneous zircon: Trace element composition as an indicator of source rock type: Contributions to Mineralogy and Petrology, v. 143, p. 602–622. 10.1007/s00410-002-0364-7.

Berberian, M., 1983, The southern Caspian: A compressional depression floored by a trapped, modified oceanic crust: Canadian Journal of Earth Sciences, v. 20, no. 2, p. 163–183. 10.1139/e83-015.

Berberian, F., and Berberian, M., 1981, Tectono-plutonic episodes in Iran, *in* Delany, F.M., and Gupta, H.K., Hindukosh, Z. eds., Himalaya geodynamic evolution: American Geophysical Union, Washington, DC, p. 5–32.

Berberian, M., and King, G.C.P., 1981, Towards a paleogeography and tectonic evolution of Iran: Canadian Journal of Earth Sciences, v. 18, no. 2, p. 210–265. 10.1139/e81-019.

Berberian, F., Muir, I.D., Pankhurst, R.J., and Berberian, M., 1982, Late Cretaceous and early Miocene Andean type plutonic activity in northern Makran and central Iran: Journal of the Geological Society of London, v. 139, no. 5, p. 605–614. 10.1144/gsjgs.139.5.0605.

Beydokhti, R., Karimpour, M.H., Mazaheri, S.A., Santos, J.F., and Klötzli, U., 2015, U-Pb zircon geochronology, sr-nd geochemistry, petrogenesis and tectonic setting of mahoor granitoid rocks (Lut Block, eastern Iran): Journal of Asian Earth Sciences, v. 111, p. 192–205. 10.1016/j.jseaes.2015.07.028.

Beydoun, Z.R., Clarke, M.W.H., and Stoneley, R., 1992, Petroleum in Zagros basin: A late tertiary foreland basin overprinted onto the outer edge of a vast hydrocarbon-rich paleozoic-Mesozoic passive-margin shelf, *in* Macqueen, R.W., and Leckie, D.A. eds., Foreland basins and fold belts: Tulsa, Oklahoma, American Association of Petroleum Geologists, p. 309–339.

Borabadi, R., Mazaheri, S.A., Karimpour, M.H., Meffre, S., Thompson, J., Murphy, R.C., and Entezariharsini, A., 2018, Zircon U-Pb geochronology, Hf isotopes and geochemistry of intrusive rocks in the Simorgh prospecting area, Lut Block, eastern Iran: Petrogenesis and geological implications: Geosciences Journal, v. 22, p. 711–732. 10.1007/s12303-017-0083-8.

Brunet, M.F., Korotaev, M.V., Ershov, A.V., and Nikishin, A.M., 2003, The south Caspian basin: A review of its evolution from subsidence modeling: Sediment Geology, v. 156, no. 1–4, p. 119–148. 10.1016/S0037-0738(02)00285-3.

Castro, A., Aghazadeh, M., Badrzadeh, Z., and Chichorro, M., 2013, Late Eocene- Oligocene post-collisional monzonitic intrusions from the Alborz magmatic belt, NW Iran. An example of monzonite magma generation from a metasomatized mantle source: Lithos, v. 180, p. 109–127. 10.1016/j.lithos.2013.08.003.

Cas, R.A.F., and Wright, J.V., 1988, Volcanic successions modern and ancient: London, Allen and Unwin. 10.1007/978-94-009-3167-1.

Chiu, H.Y., Chung, S.L., Zarrinkoub, M.H., Mohammadi, S.S., Khatib, M.M., and Iizuka, Y., 2013, Zircon U-Pb age constraints from Iran on the magmatic evolution related to Neotethyan subduction and Zagros orogeny: Lithos, v. 162, p. 70–87. 10.1016/j.lithos.2013.01.006.

Cifelli, F., Ballato, P., Alimohammadian, H., Sabouri, J., and Mattei, M., 2015, Tectonic magnetic lineation and oroclinal bending of the Alborz range: Implications on the Iran-southern Caspian geodynamics: Tectonics, v. 34, no. 1, p. 116–132. 10.1002/2014TC003626.

Cowgill, E., Forte, A.M., Niemi, N., Avdeev, B., Tye, A., Trexler, C. C., Javakhishvili, Z., Elashvili, M., and Godoladze, T.G., 2016, Relict basin closure and crustal shortening budgets during continental collision: An example from Caucasus sediment provenance: Tectonics, v. 35, p. 2918–2947. 10.1002/2016TC004295.

Dargahi, S., Arvin, M., Pan, Y., and Babaei, A., 2010, Petrogenesis of post-collisional A-type granitoids from the Urumieh-Dokhtar magmatic assemblage, Southwestern Kerman, Iran: Constraints on the Arabian–Eurasian continental collision: Lithos, v. 115, no. 1–4, p. 190–204. 10.1016/j.lithos.2009.12.002.

Davari, M., 1987, Geology, petrography, and petrology of Qasr-e-Firuzeh intrusive [M.S. thesis]: Tehran, Tehran University.

Dedual, E., 1967, Zur Geologie des Mittleren und Unteren Karaj-Tales, Zentral Elburz (Iran): Zurich: ETH Zürich Universitym: Geology Institute (in German).

Deevsalar, R., Shinjo, R., Ghaderi, M., Murata, M., Hoskin, P.W.O., Oshiro, S., Wang, K.L., Lee, H.Y., and Neill, I., 2017, Mesozoic–Cenozoic mafic magmatism in Sanandaj–Sirjan zone, Zagros orogen (western Iran): Geochemical and isotopic inferences from middle Jurassic and Late Eocene gabbros: Lithos, v. 284, p. 588–607. 10.1016/j.lithos.2017.05.009.

Dewey, J.F., Pitman, W.C., III, Ryan, W.B.F., and Bonnin, J., 1973, Plate tectonics and the evolution of the Alpine system: Geological Society of America Bulletin, v. 84, p. 3137–3180. 10.1130/0016-7606(1973)84<3137:PTATEO>2.0.CO;2.

Eftekharnejad, J., 1981, Tectonic division of Iran with respect to sedimentary basins: Journal of Iranian Petroleum Society, v. 83, p. 19–28. in Persian.

Emami, M.H., 1991, Explanatory text of the Qom quadrangle map. Geology of the quadrangle E6, Geological Survey of Iran.

Emami, M.H., 2000, Magmatism in Iran: Tehran, Geological Survey of Iran: in Persian

Förster, H., Fesefeldt, K., and Kürsten, M., 1972, Magmatic and orogenic evolution of the central Iranian volcanic belt, *in* Armstrong, J.E., and Hedberg, H.D., eds., 24th international geologic congress: International Geologic Congress, Montreal, QC, Canada, p. 198–210.

Foudazi, M., Sheikhi Karizaki, H., and Qolipour, M., 2015, Petrology and geochemistry of granitoid rocks in NW of Takestan: Scientific Quaterly Journal, Geosciences, v. 24, no. 95, p. 21–29. in Persian. 10.22071/gsj.2015.42377.

Ghasemi, A., and Talbot, C.J., 2006, A new tectonic scenario for the Sanandaj-Sirjan zone (Iran): Journal of Asian Earth Sciences, v. 26, no. 6, p. 683–693. 10.1016/j.jseaes.2005.01.003.

Guest, B., Axen, G.J., Lam, P.S., and Hassanzadeh, J., 2006, Late Cenozoic shortening in the west central Alborz Mountains, northern Iran, by combined conjugate strike-slip and thin-skinned deformation: Geosphere, v. 2, no. 1, p. 35–52. 10.1130/GES00019.1.

Guest, B., Horton, B.K., Axen, G.J., Hassanzadeh, J., and McIntosh, W.C., 2007, Middle to late Cenozoic basin evolution in the western Alborz Mountains: Implications for the onset of collisional deformation in northern Iran: Tectonics, v. 26, no. 6, p. 1–26. 10.1029/2006TC002091.

Hassanpour, S., Alirezaei, S., Selby, D., and Segeev, S., 2015, SHERIMP zircon U-Pb and biotite and hornblende ar-ar geochronology of Sungun, Haftcheshmeh, Kighal and Niaz porphyry cu-mo systems, evidence for an early Miocene porphyry-style mineralization in northwest Iran. International Journal of Earth Sciences, v. 104, p. 45–59.doi: 10.1007/s00531-014-1071-0.

Hassanzadeh, J., 1993, Metallogenic and tectono-magmatic events in the SE sector of the Cenozoic active continental margin of Iran (Shahre Babak area, Kerman province) [Ph.D. thesis]: Los Angeles, University of California.

Hassanzadeh, J., Axen, G.J., Guest, B., Stockli, D.F., and Ghazi, A. M., 2004, The Alborz and NW Urumieh-Dokhtar magmatic belts, Iran: Rifted parts of a single ancestral arc, Abstracts with Programs. GSA annual meeting, Denver.

Hassanzadeh, J., Ghazi, A.M., Axen, G., and Guest, B., 2002, Oligomiocene mafic-alkaline magmatism north and northwest of Iran: Evidence for the separation of the Alborz from the Urumieh-Dokhtar magmatic arc, GSA Annual Meeting, Denver.

Hassanzadeh, J., and Wernicke, B.P., 2016, The Neotethyan Sanandaj-Sirjan zone of Iran as an archetype for passive margin-arc transitions: Tectonics, v. 35, p. 586–621. 10.1002/2015TC003926.

Hessami, K., Koyi, H.A., Talbot, C.J., Tabasi, H., and Shabanian, E., 2001, Progressive unconformities within an evolving foreland fold-thrust belt, Zagros Mountains: Journal of the Geological Society of London, v. 158, no. 6, p. 969–981. 10.1144/0016-764901-007.

Hollingsworth, J., Fattahi, M., Walker, R., Talebian, M., Bahroudi, A., Bolourchi, M.J., Jackson, J., and Copley, A., 2010, Oroclinal bending, distributed thrust and strike-slip faulting, and the accommodation of Arabia–Eurasia convergence in NE Iran since the Oligocene: Geophysical Journal International, v. 181, no. 3, p. 1214–1246. 10.1111/j.1365-246X.2010.04591.x.

Homke, S., Vergés, J., Garcés, M., Emami, H., and Karpuz, R., 2004, Magnetostratigraphy of Miocene-Pliocene Zagros foreland deposits in the front of the Push-e Kush arc (Lurestan Province, Iran): Earth and Planetary Science Letters, v. 225, no. 3–4, p. 397–410. 10.1016/j.epsl.2004.07.002.

Honarmand, M., Rashidnejad Omran, N., Corfu, F., Emami, M.H., and Nabatian, G., 2013, Geochronology and magmatic history of a calc-alkaline plutonic complex in the Urumieh-Dokhtar Magmatic Belt, Central Iran: Zircon ages as evidence for two major plutonic episodes: Neues Jahrbuch für

Mineralogie - Abhandlungen, v. 1, p. 67–77. 10.1127/0077-7757/2013/0230.
Honarmand, M., Rashidnejad Omran, N., Neubauer, F., Emami, M.H., Nabatian, G., Liu, X., Dong, Y., Von Quadt, A., and Chen, B., 2014, Laser-ICP-MS U-Pb zircon ages and geochemical and Sr–Nd–Pb isotopic compositions of the Niyasar plutonic complex, Iran: Constraints on petrogenesis and tectonic evolution: International Geology Review, v. 56, no. 1, p. 104–132. 10.1080/00206814.2013.820375.
Jahangiri, A., 2007, Post- collisional Miocene adakitic volcanism in NW Iran: Geochemical and geodynamic implications: Journal of Asian Earth Sciences, v. 30, no. 3–4, p. 433–447. 10.1016/j.jseaes.2006.11.008.
Jamshidibadr, M., and Hassanpour, S., 2015, Geotectonic, geothermobarometry and age dating of granodiorite and granite intrusions of Shahjahan batholith: Journal of Crystallography and Mineralogy, v. 23, p. 609–622.
Jung, D., Keller, J., Khorasani, R., Marcks, C., Baumann, A., and Horn, P., 1984, Petrology of the tertiary magmatic activity in the northern Lut area, east Iran: Neues Jahrbuch Fur Geologie und Palaontologie Abhandlungen, v. 160, p. 417–467. 10.1127/njgpa/168/1984/417.
Kazmin, V.G., Sbortshikov, I.M., Ricou, L.E., Zonenshain, L.P., Boulin, J., and Knipper, A.L., 1986, Volcanic belts as markers of the Mesozoic-Cenozoic active margin of Eurasia: Tectonophysics, v. 123, no. 1–4, p. 123–152. 10.1016/0040-1951(86)90195-2.
Khademi, F., Asiabanha, A., Foden, J., and Davoodi, Z., 2019, Extensional magmatism in a continental collision zone, Tafresh area, western central Iran: structural, geochemical and mineralogical considerations: Periodico di Mineralogia, v. 88, no. 1, p. 1–18. 10.2451/2019PM822.
Kirkland, C.L., Smithies, R.H., Taylor, R.J.M., Evans, N., and McDonald, B., 2015, Zircon Th/U ratios in magmatic environs: Lithos, v. 212-215, p. 397–414. 10.1016/j.lithos.2014.11.021.
Lucci, F., Miri, M., Saki, A., White, J., Della Ventura, G., and Azizi, H., 2023, The middle Jurassic cheshmeh-ghasaban high-mg gabbro (Hamedan, NW Iran): A plume-influenced intracontinental rifting event?: Geochemistry, p. 126011. 10.1016/j.chemer.2023.126011.
Ludwig, K.R., 2003, User's Manual for Isoplot/Ex, Version 3.0, A geochronological toolkit for Microsoft Excel Berkeley Geochronology Center Special Publication, v.4, Berkeley Geochronology Center, 2455 Ridge Road, Berkeley, CA 94709, USA.
Lyberis, N., and Manby, G., 1999, Oblique to orthogonal convergence across the turan block in the post-Miocene: American Association of Petroleum Geologists Bulletin, v. 83, no. 7, p. 1135–1160. 10.1306/E4FD2E97-1732-11D7-8645000102C1865D.
Madanipour, S., Ehlers, T.A., Yassaghi, A., and Enkelmann, E., 2017, Accelerated middle Miocene exhumation of the Talesh Mountains constrained by U-Th/he thermochronometry: Evidence for the Arabia-Eurasia collision in the NW Iranian plateau: Tectonics, v. 36, no. 8, p. 1538–1561. 10.1002/2016TC004291.
Madanipour, S., Ehlers, T.A., Yassaghi, A., Rezaeian, M., Enkelmann, E., and Bahroudi, A., 2013, Synchronous deformation on the orogenic plateau margins, insights from the Arabia-Eurasia collision: Tectonophysics, v. 608, p. 440–451. 10.1016/j.tecto.2013.09.003.
Mahmoudi, S., Corfu, F., Masoudi, F., Mehrabi, B., and Mohajjel, M., 2011, U-Pb dating and emplacement history of granitoid plutons in the northern Sanandaj-Sirjan zone, Iran: Journal of Asian Earth Sciences, v. 41, no. 3, p. 238–249. 10.1016/j.jseaes.2011.03.006.
Mattei, M., Cifelli, F., Alimohammadian, H., Rashid, H., Winkler, A., and Sagnotti, L., 2017, Oroclinal bending in the Alborz Mountains (northern Iran): New constraints on the age of south Caspian subduction and extrusion tectonics: Gondwana Research, v. 42, p. 13–28. 10.1016/j.gr.2016.10.003.
Mazhari, S.A., Amini, S., Ghalamghash, J., and Bea, F., 2011, Petrogenesis of granitic unit of Naqadeh complex, Sanandaj-Sirjan Zone, NW Iran: Arabian Journal of Geosciences, v. 4, no. 1, p. 59–67. 10.1007/s12517-009-0077-6.
Mazhari, S.A., Bea, F., Amini, S., Ghalamghash, J., Molina, J.F., Montero, P., Scarrow, J.H., and Williams, I.S., 2009, The Eocene bimodal Piranshahr massif of the Sanandaj-Sirjan zone, NW Iran: A marker of the end of the collision in the Zagros orogen: Journal of the Geological Society of London, v. 166, no. 1, p. 53–69. 10.1144/0016-76492008-022.
McCall, G.J.H., 1997, The geotectonic history of the Makran and adjacent area of southern Iran: Journal of Asian Earth Sciences, v. 15, p. 517–531. 10.1016/S0743-9547(97)000329.
McFarlane, C., and Luo, Y., 2012, U-Pb geochronology using 193 nm excimer LA-ICP-MS optimized for in situ accessory mineral dating in thin sections: Geoscience Canada, v. 39, no. 3, p. 158–72.
McQuarrie, N., Stock, J.M., Verdel, C., and Wernicke, B.P., 2003, Cenozoic evolution of Neotethys and implications for the causes of plate motions: Geophysical Research Letters, v. 30, no. 20, p. 2036. 10.1029/2003GL017992.
McQuarrie, N., and Van Hinsbergen, D.J., 2013, Retro-deforming the Arabia-Eurasia collision zone: Age of collision versus magnitude of continental subduction: Geology, v. 41, no. 3, p. 315–318. 10.1130/G33591.1.
Miskovic, A., and Schaltegger, U., 2009, Crustal growth along a non-collisional cratonic margin: A Lu–Hf isotopic survey of the eastern Cordilleran granitoids of Peru: Earth and Planetary Science Letters, v. 279, no. 3–4, p. 303–315. 10.1016/j.epsl.2009.01.002.002.
Mohajjel, M., Fergusson, C.L., and Sahandi, M.R., 2003, Cretaceous-tertiary convergence and continental collision, Sanandaj-Sirjan Zone, western Iran: Journal of Asian Earth Sciences, v. 21, no. 4, p. 397–412. 10.1016/S1367-9120(02)00035-4.
Morley, C.K., Kongwung, B., Julapour, A.A., Abdolghafourian, M., Hajian, M., Waples, D., Warren, J., Otterdoom, H., Srisuriyon, K., and Kazemi, H., 2009, Structural development of a major late Cenozoic basin and transpressional belt in central Iran: The central basin in the Qom-Saveh area: Geosphere, v. 5, no. 4, p. 325–362. 10.1130/GES00223.1.
Nabatian, G., Ghaderi, M., Neubauer, F., Honarmand, M., Liu, X., Dong, Y., Jiang, S.Y., Quadt, A., and Bernroider, M., 2014, Petrogenesis of Tarom high-potassic granitoids in the Alborz–azarbaijan belt, Iran: Geochemical, U-Pb zircon and sr-nd-Pb isotopic constraints: Lithos, v. 184, p. 324–345. 10.1016/j.lithos.2013.11.002.
Nadirov, R.S., Bagirov, M., Tahiyev, M., and Lerche, I., 1997, Flexural plate subsidence, sedimentation rates, and structural development of the super-deep south Caspian basin:

Marine and Petroleum Geology, v. 14, no. 4, p. 383–400. 10.1016/S0264-8172(96)00054-2.

Nasrabady, M., Rossetti, F., Theye, T., and Vignaroli, G., 2011, Metamorphic history and geodynamic signify cance of the Early Cretaceous Sabzevar granulites (Sabzevar structural zone, NE Iran): Advances in Fission-Track Geochronology, v. 2, p. 219–243. 10.5194/se-2-219-2011.

Nazarinia, A., Mortazavi, M., Arvin, M., Hu, R., Zhao, C., and Poosti, M., 2018, U-Pb zircon dating, sr-nd isotope and petrogenesis of sarduiyeh granitoid in SE of the UDMA, Iran: Implication for the source origin and magmatic evolution: International Geology Review, v. 62, no. 13–14, p. 1796–1814. 10.1080/00206814.2018.1514668.

Omidianfar, S., Rahgoshay, M., and Monsef, I., 2018, Mineralogy, geochemistry and tectonic setting of Paleogene volcanic lavas in the southwest of basiran (east of Lut block, east of Iran): Petrology, v. 9, p. 183–204. in Persian.

Omrani, J., Agard, P., Whitechurch, H., Benoit, M., Prouteau, G., and Jolivet, L., 2008, Arcmagmatism and subduction history beneath the Zagros Mountains, Iran: A new report of adakites and geodynamic consequences: Lithos, v. 106, no. 3–4, p. 380–398. 10.1016/j.lithos.2008.09.008.

Omrani, H., Moazzen, M., Oberhänsli, R., Altenberger, U., and Lange, M., 2013, The Sabzevar blueschists of the north-central Iranian micro-continent as remnants of the Neotethys-related oceanic crust subduction: International Journal of Earth Sciences, v. 102, no. 5, p. 1491–1512. 10.1007/s00531-013-0881-9.

Pang, K.N., Chung, S.L., Zarrinkoub, M.H., Khatib, M.M., Mohammadi, S.S., Lee, H.Y., Chu, C.H., and Lin, I.J., 2011, Eocene-Oligocene calc-alkaline magmatism in the Lut-Sistan region, eastern Iran: Petrogenesis and tectonic implications: AGU Fall Meeting Abstracts, p. V43C–2598.

Pang, K.N., Chung, S.L., Zarrinkoub, M.H., Mohammadi, S.S., Yang, H.M., Chu, C.H., Lee, H.Y., and Lo, C.H., 2012, Age, geochemical characteristics and petrogenesis of Late Cenozoic intraplate alkali basalts in the Lut-Sistan region, eastern Iran: Chemical Geology, v. 306, p. 40–53. 10.1016/j.chemgeo.2012.02.020.

Polliand, M., Schaltegger, U., Frank, M., and Fontboté, L., 2005, Formation of intra-arc volcano sedimentary basins in the western flank of the central Peruvian andes during Late Cretaceous oblique subduction: Field evidence and constraints from U-Pb ages and Hf isotopes: International Journal of Earth Sciences, v. 94, p. 231–242. 10.1007/s00531-005-0464-5.

Rabiee, A., Rossetti1, F., Asahara, Y., Azizi, H., Lucci1, F., Lustrino, M., and Nozaem, R., 2020, Long lived, Eocene-Miocene stationary magmatism in NW Iran along a transform plate boundary: Gondwana Research, v. 85, p. 237–262. 10.1016/j.gr.2020.03.014.

Rabiee, A., Rossetti, F., Lucci, F., and Lustrino, M., 2022, Cenozoic porphyry and other hydrothermal ore deposits along the south Caucasus-west Iranian tectono-magmatic belt: A critical reappraisal of the controlling factors: Lithos, v. v, p. 430–431, 106874. 10.1016/j.lithos.2022.106874.

Rabiee, A., Rossetti, F., Tecce, F., Asahara, Y., Azizi, H., Glodny, J., Lucci, F., Nozaem, R., Opitz, J., and Selby, D., 2019, Multiphase magma intrusion, ore-enhancement and hydrothermal carbonatisation in the Siah-Kamar porphyry mo deposit, Urumieh-Dokhtar magmatic zone, NW Iran: Ore Geology Reviews, v. 110, p. 102930. 10.1016/j.oregeorev.2019.05.016.

Rezaeian, M., 2008, Coupled tectonics, erosion and climate in the Alborz Mountains, Iran [Ph.D. thesis]]: Cambridge, University of Cambridge.

Rezaeian, M., Carter, A., Hovius, N., and Allen, M.B., 2012, Cenozoic exhumation history of the Alborz Mountains, Iran: New constraints from low-temperature chronometry: Tectonics, v. 31, no. 2, p. 1–20. 10.1029/2011TC002974.

Rezaei, F., Azizi, H., and Asahara, Y., 2021, Tectonic significance of the late Eocene (Bartonian) calc-alkaline granitoid body in the Marivan area, Zagros suture zone, northwest Iran: International Geology Review, v. 64, no. 8, p. 1–16. 10.1080/00206814.2021.1907624.

Richards, J.P., 2003, Metallogeny of the Neo-Tethys arc in central Iran, *in* Eliopoulos et al. eds., mineral exploration and sustainable development. 7th biennial SGA meeting, Athens, au-gust 24—28: Millpress, Rotterdam, p. 1237–1239.

Rolland, Y., 2017, Caucasus collisional history: Review of data from east Anatolia to west Iran: Gondwana Research, v. 49, p. 130–146. 10.1016/j.gr.2017.05.005.

Rossetti, F., Nasrabady, M., Vignaroli, G., Theye, T., Gerdes, A., Razavi, S.M.H., and Moin Vaziri, H., 2010, Early Cretaceous migmatitic mafi c granulites from the Sabzevar range (NE Iran): Implications for the closure of the Mesozoic peri-Tethyan oceans in central Iran: Terra Nova, v. 22, p. 26–34. 10.1111/j.1365-3121.2009.00912.x.

Saccani, E., Delavari, M., Beccaluva, L., and Amini, S., 2010, Petrological and geochemical constraints on the origin of the nehbandan ophiolitic complex (eastern Iran): Implication for the evolution of the Sistan Ocean: Lithos, v. 117, p. 209–228. 10.1016/j.lithos.2010.02.016.

Sarjoughian, F., and Kananian, A., 2017, Zircon U-Pb geochronology and emplacement history of intrusive rocks in the Ardestan section, central Iran: Geologica Acta, v. 15, no. 1, p. 25–36. 10.1344/GeologicaActa2017.15.1.3.

Schaltegger, U., Fanning, C.M., Günther, D., Maurin, J.C., Schulmann, K., and Gebauer, D., 1999, Growth, annealing and recrystallization of zircon and preservation of monazite in high-grade metamorphism: Conventional and in-situ U-Pb isotope, cathodoluminescence and microchemical evidence: Contributions to Mineralogy and Petrology, v. 134, p. 186–201. 10.1007/s004100050478.

Schellart, W.P., 2005, Influence of the subducting plate velocity on the geometry of the slab and migration of the subduction hinge: Earth and Planetary Science Letters, v. 231, no. 3–4, p. 197–219. 10.1016/j.epsl.2004.12.019.

Sengör, A.M.C., Altiner, D., Cin, A., Ustaomer, T., and Hsu, K.J., 1988, Origin and assembly of the Tethyside orogenic collage at the expense of Gondwana land, *in* Audley-Charles, M.G., and Hallam, A., eds., Gondwana and tethys: London, Journal of the Geological Society of London, Special publication, p. 119–181.

Sepahi, A.A., Shahbazi, H., Siebel, W., and Ranin, A., 2014, Geochronology of plutonic rocks from the Sanandaj-Sirjan zone, Iran and new zircon and titanite U-Th-Pb ages for granitoids from the Marivan pluton: Geochronometria, v. 41, p. 207–215. 10.2478/s13386-013-0156-z.

Sepidbar, F., Shafaii Moghadam, H., Zhangc, L., Li, J.W., Ma, J., Stern, R.J., and Lin, C., 2019, Across-arc geochemical variations in the Paleogene magmatic belt of Iran: Lithos, v. 344, p. 280–296. 10.1016/j.lithos.2019.06.022.

Shafaii Moghadam, H., Corfu, F., and Stern, R.J., 2013, U-Pb zircon ages of Late Cretaceous Nain–dehshir ophiolites, central Iran: Journal of the Geological Society of London, v. 170, p. 175–184. 10.1144/jgs2012-066.

Shafaii Moghadam, H., Griffin, W., Kirchenbaur, M., Garbe-Schönberg, D., Zaki Khedr, M., Kimura, J.I., Stern, B., Ghorbani, G., Murphy, R., O'Reilly, S.Y., Arai, S., and Maghdour-Mashhour, R., 2018, Roll-back, extension and mantle upwelling triggered Eocene potassic magmatism in NW Iran: Journal of Petrology, v. 59, no. 7, p. 1417–1465. 10.1093/petrology/egy067.

Shafaii Moghadam, H., Griffin, W., Santos, J.F., Chen, R.X., Karsli, O., Lucci, F., Sepidbar, F., and O'Reilly, S.Y., 2022, Geochronology, geochemistry and petrology of the Oligocene magmatism in SE segment of the UDMB, Iran: Lithos, v. v, p. 416–417, p. 106644. 10.1016/j.lithos.2022.106644.

Shafaii Moghadam, H.S., Khademi, M., Hu, Z.C., Stern, R.J., Santos, J.F., and Wu, Y.B., 2015, Cadomian (Ediacaran-Cambrian) arc magmatism in the ChahJam-biarjmand metamorphic complex (Iran): Magmatism along the northern active margin of Gondwana: Gondwana Research, v. 27, no. 1, p. 439–452. 10.1016/j.gr.2013.10.014.

Shafaii Moghadam, H., Li, Q.L., Griffin, W.L., Stern, B., Santos, J.F., Ducea, M.N., Ottley, C.J., Karsli, O., Sepidbar, F., and O'Reilly, S.Y., 2022, Temporal changes in subduction- to collision-related magmatism in the Neotethyan orogen: The southeast Iran example: Earth Science Review, v. 226, no. Article 103930, p. 1–19. 10.1016/j.earscirev.2022.103930.

Shafaii Moghadam, H., Li, Q.L., Li, X.H., Chiaradia, M., Karsli, O., Hoernle, K.A., and Griffin, W.L., 2023, Mantle-derived high-K magmatic fluxes in northeast Iran arc: Constraints from zircon U-Pb-O-Hf and bulk rock major-trace elementsand sr-nd-Pb isotopes: Gondwana Research, v. 119, p. 1–26. 10.1016/j.gr.2023.02.021.

Shafaii Moghadam, H., Rossetti, F., Lucci, F., Chiaradia, M., Gerdes, A., Martinez, M.L., Ghorbani, G., and Nasrabady, M., 2016, The calc-alkaline and adakitic volcanism of the Sabzevar structural zone (NE Iran): implications for the Eocene magmatic flare-up in Central Iran: Lithos, v. 248, p. 517–535. 10.1016/j.lithos.2016.01.019.

Shafaii Moghadam, H.S., and Stern, R.J., 2011, Geodynamic evolution of upper cretaceous Zagros ophiolites: Formation of oceanic lithosphere above a nascent subduction zone: Geological Magazine, v. 148, no. 5–6, p. 762–801. 10.1017/S0016756811000410.

Shafaii Moghadam, H., Whitechurch, H., Rahgoshay, M., and Monsef, I., 2009, Significance of Nain-baft ophiolitic belt (Iran): Short-lived, transtensional Cretaceous back-arc oceanic basins over the Tethyan subduction zone: Comptes Rendus Geoscience, v. 341, p. 1016–1028. 10.1016/j.crte.2009.06.011.

Shahabpour, J., 2007, Island-arc affinity of the central Iranian volcanic belt: Journal of Asian Earth Science, v. 30, no. 5–6, p. 652–665. 10.1016/j.jseaes.2007.02.004.

Shahbazi, H., Sepahi, A.A., and Shakouri, A., 2021, Zircon U-Pb ages and petrogenesis of the middle Eocene Aliabad Daman pluton, Northeast Iran: Implications for magmatic activity along the Doruneh fault zone: Arabian Journal of Geosciences, v. 14, p. 1–21. 10.1007/s12517-020-06437-w.

Sláma, J., Košler, J., Condon, D.J., Crowley, J.L., Gerdes, A., Hanchar, J.M., Horstwood, M.S.A., Morris, G.A., Nasdala, L., Norberg, N., Schaltegger, U., Schoene, B., Tubrett, M.N., and Whitehouse, M.J., 2008, Plešovice zircon - A new natural reference material for U-Pb and Hf isotopic microanalysis: Chemical Geology, v. 249, no. 1–2, p. 1–35. 10.1016/j.chemgeo.2007.11.005.

Spies, O., Lensch, G., and Mihm, A., 1984, Petrology and geochemistry of the post-ophiolitic Tertiary volcanics between Sabzevar and Quchan, NE Iran: Neues Jurbuch Fur Geologie und Palaontologie-Abhandlungen, v. 168, p. 389–408. 10.1127/njgpa/168/1984/389.

Stampfli, G.M., and Borel, G.D., 2002, A plate tectonic model for the Paleozoic and Mesozoic constrained by dynamic plate boundaries and restored synthetic oceanic isochrons: Earth and Planetary Science Letters, v. 196, no. 1–2, p. 17–33. 10.1016/S0012-821X(01)00588-X.

Stern, R.J., Shafaii Moghadam, H., Pirouz, M., and Mooney, W., 2021, The geodynamic evolution of Iran: Annual Review of Earth and Planetary Sciences, v. 49, p. 9–36. 10.1146/annurev-earth-071620-052109.

Stöcklin, J., 1968, Structural history and tectonics of Iran: A review: American Association of Petroleum Geologists Bulletin, v. 52, no. 7, p. 1229–1258. 10.1306/5D25C4A5-16C1-11D7-8645000102C1865D.

Van der Boon, A., van Hinsbergen, D.J.J., Rezaeian, M., Gürer, D., Honarmand, M., Pastor- Galán, D., Krijgsman, W., and Langereis, C.G., 2018, Quantifying Arabia–Eurasia convergence accommodated in the greater Caucasus by paleomagnetic reconstruction: Earth and Planetary Science Letters, v. 482, p. 454–469. 10.1016/j.epsl.2017.11.025.

Verdel, C.S., Wernicke, B.P., Hassanzadeh, J., and Guest, B., 2011, A Paleogene extensional arc flare-up in Iran: Tectonics, v. 30, no. 3, p. 1–20. 10.1029/2010TC002809.

Verdel, C., Wernicke, B.P., Ramezani, J., Hassanzadeh, J., Renne, P.R., and Spell, T.L., 2007, Geology and thermochronology of tertiary Cordilleran-style metamorphic core complexes in the Saghand region of central Iran: Geological Society of America Bulletin, v. 119, no. 7–8, p. 961–977. 10.1130/B26102.1.

Vincent, S.J., Allen, M.B., Ismail-Zadeh, A.D., Flecker, R., Foland, K.A., and Simmons, M.D., 2005, Insights from the Talysh of Azerbaijan into the Paleogene evolution of the south Caspian: Geological Society of America Bulletin, v. 117, no. 11–12, p. 1513–1533. 10.1130/B25690.1.

Vincent, S.J., Morton, A.C., Carter, A., Gibbs, S., and Barabadze, T.G., 2007, Oligocene uplift of the western greater Caucasus: An effect of initial Arabia–Eurasia collision: Terra Nova, v. 19, no. 2, p. 160–166. 10.1111/j.1365-3121.2007.00731.x.

Whitney, D.L., and Evans, B.W., 2010, Abbreviations for names of rock-forming minerals: American Mineralogist, v. 95, no. 1, p. 185–187. 10.2138/am.2010.3371.

Zarrinkoub, M.H., Chung, S.L., Chiu, H.Y., Mohammadi, S.S., Khatib, M.M., and Lin, I.J., 2010, Zircon U-Pb age and geochemical constraints from the northern Sistan suture zone on the Neotethyan magmatic and tectonic evolution in eastern Iran, *in* Dilet, Y., ed., Tectonic crossroads: Evolving orogens of Eurasia–Africa–Arabia, Ankara, Turkey: Boulder, Colorado, USA: Geological Society of America. p. 54. Abstract Volume.

Zarrinkoub, M.H., Pang, K.N., Chung, S.L., Khatib, M.M., Mohammadi, S.S., Chiu, H.Y., and Lee, H.Y., 2012, Zircon U-Pb ages and geochemical constraints on the origin of the Birjand ophiolite, eastern Iran: Lithos, v. 154, p. 392–405. 10.1016/j.lithos.2012.08.007.